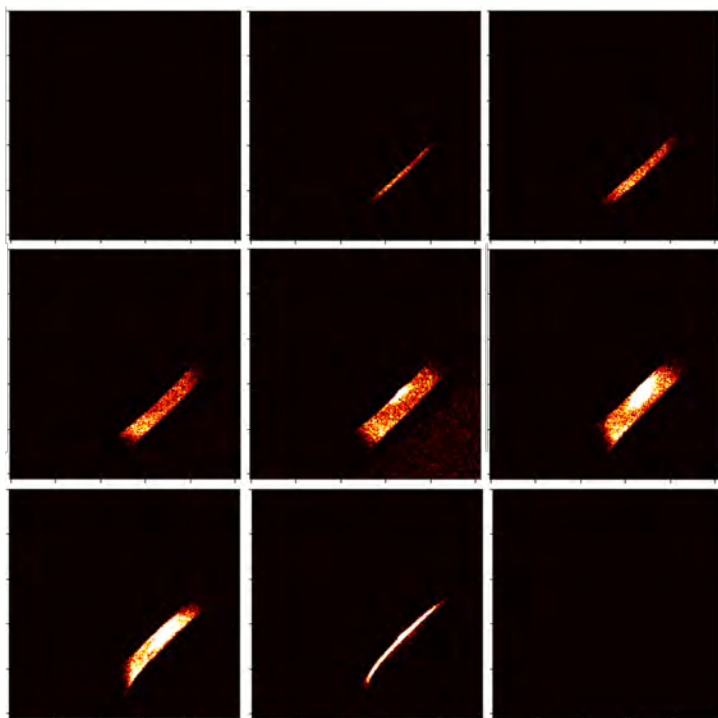


Master Thesis

Photon-induced near-field electron microscopy in a Scanning Electron Microscope

A thesis submitted by
Hannah Niese



Thesis Advisors:
Matthias Liebtrau
Prof. Dr. Albert Polman
Photonic Materials Group
FOM-Institute for Atomic and Molecular Physics (AMOLF)

Examiner at ETH Zürich
Prof. Dr. David J. Norris

April 22, 2022

Abstract

The interaction of free electrons with light and matter offers new ways to characterize materials and nanophotonic systems and in particular nanophotonic systems at attosecond time and nanometer length scales over an ultra wide spectral range. When swift electrons pass through a photon-induced near-field of a nanostructure, PINEM (Photon-induced near-field electron microscopy) can be observed, where the electron interacts with the near-fields and gains or loses energy quanta of the photon. We worked on a setup for energy-resolved single-electron detection to measure PINEM with non-relativistic electrons in a Scanning electron microscope (SEM).

We modified and characterized a Retarding Field Analyzer (RFA) in experiments and simulations, which revealed an intrinsic energy resolution down to 100meV for incident electron energies of 4-6 keV. We introduce a silicon-based single-electron detector that can detect extremely small electron signals down to an effective beam current on the order of a few hundred attoamperes, but also detects signal from the laser in the setup. To block laser light from reaching the sensor surface and thus obscuring the electron signal, we design and test a deflection unit that only allows electrons through to the sensor. Nanostructures that can be used to show PINEM in our experimental conditions were simulated using Finite Difference Time-Domain (FDTD) methods, and PINEM coupling parameters and expected PINEM spectra were calculated for the nanostructures that were used in experiments.

Acknowledgment

I want to thank Albert for inviting me to your group and to Amsterdam, a real adventure and opportunity to grow scientifically as well as personally. Matthias, thanks for supervising me on this project and introducing me to the world of free-electrons (and all of the instrumentation). I enjoyed working with you in the lab, as well as on simulations and the analysis. Thanks for always being available for questions and feedback, or to debug some scripts.

I was glad we could collaborate with many technical specialists, our group technician Dion Ursem who was always quick come up with smart ideas and to fix things, Bob Krijger from the electronics department without whose custom-made electronics we couldn't have done any experiment at all, and Max Postma from the mechanical engineering department who came up with great engineering solutions and did all the construction for the parts that we designed.

Finally, my thanks go to all the members of the Photonic Materials group who welcomed me so warmly to AMOLF. Matthias, Nika, Stefan, Andrea, Magda, Tom, Evelijn, Hollie, Heleen, Dion and Albert it was a pleasure working with you!

Table of Contents

1	Introduction	7
2	Nanophotonic Simulations	13
2.1	Theory	13
2.2	Nanostructures	14
2.3	Simulation setup	15
2.4	Results	16
2.5	Interaction for different electron energies	18
3	Detector Development	19
3.1	Energy Analyzer	19
3.2	MiniPix Detector	24
3.3	Deflection Unit	27
3.3.1	Electron Trajectory Calculations	29
3.3.2	Simulation Results	31
4	Results	35
4.1	Retarding Field Analyzer	35
4.2	Deflection Unit	38
4.3	Electron Energy Spectra	40
4.4	Sample Damage	42
5	Conclusion and outlook	45
A	Setting up an experiment	47

B Data sets	50
C MiniPix Detection	52
D Code	53
D.1 Electron Trajectories	53
D.2 SIMION script	53
E Technical Drawings	55
Bibliography	75
List of Figures	78
List of Tables	79
Declaration of originality	81

Chapter 1

Introduction

Nanophotonics - the manipulation of light with nanoscale structures has a wide range of applications in spectroscopy, catalysis, nanofabrication, optical communication, photovoltaics and many more ([Koenderink et al., 2015](#)). To study the underlying phenomena and develop new technological applications, there is a crucial demand for suitable optical characterization methods. However, the resolution of typical optical microscopy approaches is fundamentally limited by diffraction ([Abbe, 1873](#)). That means that structures and phenomena at length scales smaller than the wavelength of the radiation source cannot be resolved - for the case of visible light this is in range of a few hundred nanometers. Electron microscopy overcomes this limit by using accelerated electrons - which enable resolutions down to atomic length scales. Due to wave-particle duality, electrons can be described by their energy, velocity and de Broglie wavelength¹, some examples are listed in [Table 1.1](#). Velocities range from comparatively slow electrons to electrons moving at almost 70% of the speed of light, where relativistic effects become important. This wide range of energies renders electron microscopy a very versatile characterization tool.

Energy [keV]	Wavelength λ [pm]	Velocity v [m/s]	fraction of speed of light $\beta = v/c$
1keV	38.764	$1.8728 \cdot 10^7$	0.06247
4keV	19.391	$3.7292 \cdot 10^7$	0.12439
5keV	17.344	$4.1633 \cdot 10^7$	0.13887
6keV	15.833	$4.5541 \cdot 10^7$	0.15191
7.5keV	14.161	$5.08061 \cdot 10^7$	0.16947
10keV	12.205	$5.8455 \cdot 10^7$	0.19499
20keV	8.5885	$8.1503 \cdot 10^7$	0.27187
30keV	6.9791	$9.8445 \cdot 10^7$	0.32838
100keV	3.7014	$1.6435 \cdot 10^8$	0.54822
200keV	2.5079	$2.0845 \cdot 10^8$	0.69531

Table 1.1: Wavelengths and velocities of electrons at different acceleration voltages

Interestingly, in recent years free electrons have been shown to not only enable high-resolution structural measurements, but also correlated optical measurements in nanophotonics ([De Abajo, 2010](#); [Losquin and Lummen, 2017](#); [Polman et al., 2019](#); [Di Giulio et al., 2019](#); [Garcia de Abajo](#)

¹ $\lambda = \frac{h}{\gamma m v}$ where γ is the Lorentz factor, m the electron's rest mass and v its velocity

and Di Giulio, 2021). From the point of view of electrodynamics, the electron can be described as a moving point charge accompanied by an associated evanescent electromagnetic field. When the electron experiences a change in the dielectric environment close to its trajectory - as it is passing by close to a structure - these fields polarize the material and act as a source of optical excitation (De Abajo, 2010; Polman et al., 2019; Coenen and Haegel, 2017). This process can occur within a fraction of a femtosecond, which corresponds to a broad frequency spectrum (entire ultraviolet-visible-near-infrared spectral range), distinguishing the electron from conventional light sources such as lasers.

This property has rendered electrons a powerful characterization tool to investigate optical properties of materials and structures with high spatial, temporal and energy resolution (De Abajo, 2010; Losquin and Lummén, 2017; Polman et al., 2019). The electron interacts with its self-induced field. For example, we can probe how efficiently electrons transfer energy to individual electromagnetic excitations using Electron energy-loss spectroscopy (EELS) (Egerton et al., 2005). We can further observe the radiative decay of such a self-induced field with Cathodoluminescence (CL) spectroscopy (Coenen and Haegel, 2017).

Recently, it has been shown that free electrons can also interact with electromagnetic fields that are driven by an external source, such as a laser (Barwick et al., 2009; García de Abajo et al., 2010; Park et al., 2010). This interaction also permits the electron to gain energy (EEGS) (de Abajo and Kociak, 2008), and is referred to as electron-energy gain spectroscopy, or photon-induced near-field electron microscopy (PINEM).

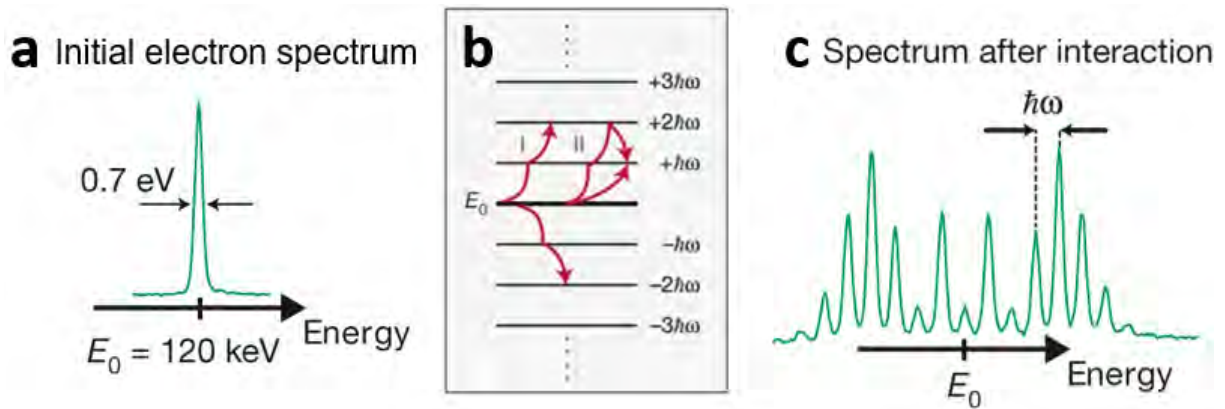


Figure 1.1: PINEM energy spectrum of electrons measured before (left) and after (right) the interaction with the nanostructure (middle) (Feist et al., 2015).

A first report by Barwick et al. (2009) demonstrated PINEM by probing the near-fields of a carbon nanotubes and silver nanowires. Theoretical explanations by García de Abajo et al. (2010) and experimental work by (Feist et al., 2015) established the quantum nature of PINEM. Electron energy spectra before and after passing the optical near-field of a gold nanotip as taken from Feist et al. (2015) can be seen in Figure 1.1. The initial electron spectrum consists of a single peak around the initial electron energy E_0 (Figure 1.1a). While the electron passes through the quantized near-field, it undergoes one or more energy-gain or energy-loss transitions by absorption or emission of photons of the laser frequency ω - i.e. it climbs up and down discrete steps of a quantum ladder, as illustrated in Figure 1.1b. After the interaction (Figure 1.1c), one can see the emergence of several side-bands, with spacing of integer multiples of $\hbar\omega$ from the initial zero-loss peak. (Park et al., 2010; García de Abajo et al., 2010).

The correspondence between EELS, CL and PINEM as a family of phenomena was studied experimentally by [Liebtrau et al. \(2021\)](#) on gold nanostars, which were investigated in an SEM (CL) and an ultrafast Transmission Electron Microscope (TEM, for EELS, PINEM).

Experimental observations of PINEM present several challenges, requiring a well-controlled electron beam and the ability to measure the energy of the electron after its interaction with the optical near-field. In TEMs, commercially available EELS spectrometers that provide the necessary high energy resolution are already widely used in setups ([Feist et al., 2015](#); [Vanacore et al., 2018](#); [Wang et al., 2020](#)). SEMs, on the other hand are mainly built for imaging applications, where Secondary Electrons (SE) or Backscattered Electrons (BSE) are collected above the sample to reconstruct an image. Advances have been made to also measure in transmission in SEMs, where EELS detectors with good energy resolutions are advertised (0.4 eV and 0.5 eV at 30keV [Sunaoshi et al. \(2016\)](#); [Brodusch et al. \(2019\)](#)), however, for single-digit keV ranges there are no commercially available solutions with sufficiently high energy resolution available.

Not only the detection is challenging, but also inducing the effect in the first place, as it requires very high field intensities in the nanostructure. These kinds of fields can be provided by pulsed lasers, which supply high intensities during short times, also requiring a pulsed electron beam which is temporally synchronized with the laser pulses ([García de Abajo et al., 2010](#)). Usually this is done with a setup that is exploiting the photoelectric effect to release electrons from the electron source in the microscope, using a higher harmonic of a pulsed laser that is simultaneously used for the optical excitation of the nanostructure. These pulse are in the femtosecond range, and can be synchronised with optical delay lines ([Solà Garcia, 2021](#); [Feist et al., 2017](#)).

Strong PINEM has also been observed with continuous-wave (CW) laser excitation. In that case, cavities with very high Q-factors are used to provide the strong fields that are necessary ([Henke et al., 2021](#); [Dahan et al., 2021](#)).

All PINEM measurements have been done in TEMs using relativistic electrons, except [Shiloh et al. \(2021\)](#), who measured PINEM at 17.4 keV and 10.4 keV, with a home-built detector based on an Omega filter.

However, sub-relativistic electrons (down to a few hundred eV) were shown to promise high electron-light coupling efficiencies ([Talebi, 2019](#); [Liebtrau et al., 2021](#)). The highest coupling efficiencies are found where the fields are most concentrated spatially. These high spatial Fourier components are only accessible for slow electrons, which have a large wave vector q . Working with sub-relativistic has the additional advantage that a much larger range of velocities is available (see [Table 1.1](#)), ranging from 6% of the speed of light at 1 keV to 32% at 30 keV, while there is a lower velocity difference for relativistic electrons (55% at 100 keV to 69% at 200 keV).

Furthermore, SEM chambers can be much larger than typical TEM chambers which allows to build flexible and more complex setups. One such experiment is building free-electron qubits, which would consist of a number of nanostructures stacked on top of one another ([Reinhardt et al., 2021](#)).

In this work we follow a completely different approach: We use a different energy-resolved detection system, and while we also use a pulsed laser, we employ a different mechanism to create and synchronise the electron wave packets. We avoid the complex laser system and

alignment procedures by using an electrostatic beam blanker that chops the beam by sweeping it across a small aperture, producing electron pulses as short as a few of tens of picoseconds. In this configuration and at these timescales, all the delay lines can be done electronically (Meuret et al., 2019).

A schematic overview of our setup can be seen in Figure 1.2. We use an SEM instrument (FEI Quanta FEG 650, Thermo Fisher Scientific Inc.) equipped with a Schottky field emission electron source and modified with an electrostatic beam blanker and a final aperture of $70\ \mu\text{m}$ diameter to chop the sweeping beam. A dual channel function generator (Keysight, Trueform 33600A) is used to send a square wave signal to the beam blanker and to a pulsed trigger signal to a Nd:YVO₄ laser (InnoLas Picolo). The two output channels are internally synchronised with negligible jitter and the laser trigger signal is delayed by a digital delay generator (Stanford Research Systems DG645). Using a fast Si photodiode (Hamamatsu S5971), the arrival of electrons and photons is measured and visualized on a high-bandwidth oscilloscope (Rhode & Schwarz RTO6 2GHz), and the delay can be adjusted to ensure temporal overlap.

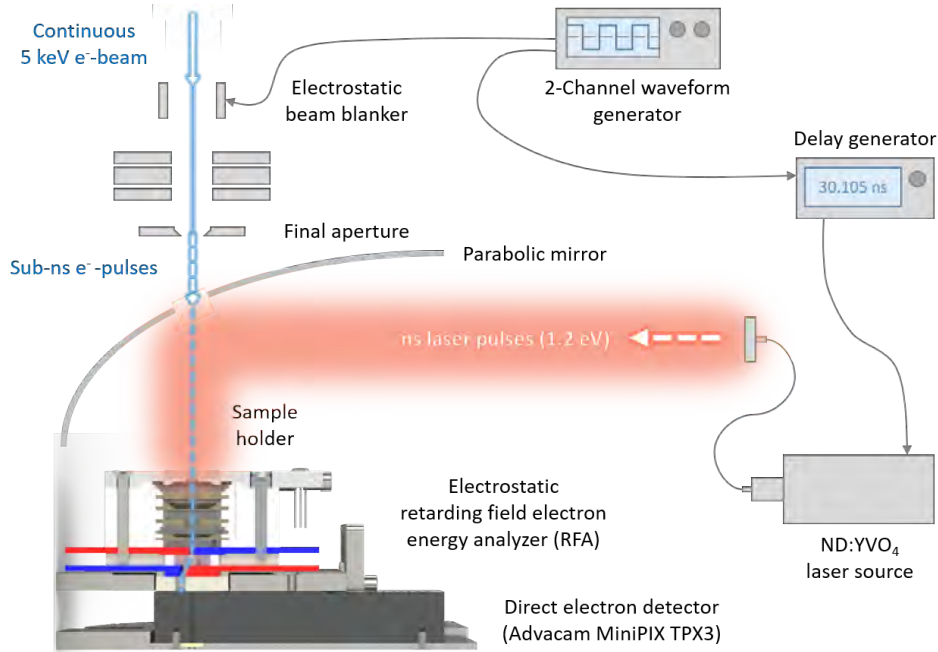


Figure 1.2: Overview of the setup with the electrons indicated in blue and the laser in red.

The laser is coupled into the chamber via an optical fibre and focussed onto the nanostructure using a commercial cathodoluminescence light collection setup (DELMIC BV), which consists of a fibre-coupling unit, a series of optics and a half-parabolic mirror. This system is usually used to couple out CL signal to an external spectrometer, and is used here in the reverse direction.

The detection of electrons at low non-relativistic kinetic energies on the order of a few keV is one of the main challenges in this setup. For example, if the laser is used with a repetition rate of 25 kHz and 800 ps pulse duration, this equates to a duty cycle of $2 \cdot 10^{-5}$. The electron pulses need to be matched with this duty cycle, which means that when we can expect a typical beam current of 1 nA under standard operation conditions, in pulsed conditions this is reduced to $2 \cdot 10^{-14}\text{A}$, or 20 fA. Depending on the interaction efficiency, again only a fraction of these electrons contribute to the PINEM side-bands, requiring the detection of electron

signals with a resolution on the order of a few tens to hundreds of attoamperes. Modern commercial EELS spectrometers are capable of detecting such low signals, however they are not suited for the low electron energies that we use in our experiments.

In this thesis, we developed a detection and measurement system that can be seen in [Figure 1.3](#) and is described in detail in the following chapters. First, in [chapter 2](#), we use numerical near-field simulations to characterize the suitability of a nanohole array for PINEM experiments with electron energies of a few keV in the SEM. Then, we go to the electron detection subsystem in [chapter 3](#), which is the focus of this thesis. We simulate and characterize a Retarding Field Analyzer and ensure that we can reach high energy resolutions. Furthermore, we introduce a sensitive single-electron detector that enables measurement of extremely small currents of low-energy electrons. This detector is so sensitive that it detects signal from the laser and the electrons, therefore we design a deflection unit to solve this problem. In [chapter 4](#) the detection performance of each of the components and the entire system is tested. Finally, in [chapter 5](#) we discuss and give an outlook.

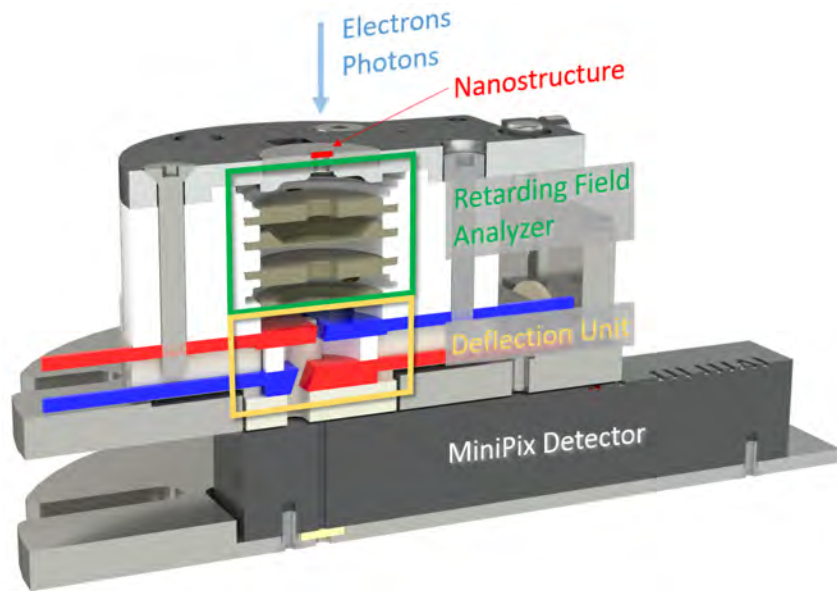


Figure 1.3: Overview of the detection system, consisting of the nanostructure ([chapter 2](#)), Retarding Field Analyzer ([section 3.1](#)) and Deflection Unit ([section 3.3](#)) and the MiniPix Detector ([section 3.2](#)).

Chapter 2

Nanophotonic Simulations

2.1 Theory

In free space, the interaction between electrons and photons is forbidden by energy-momentum conservation. In the presence of a nanostructure and an external excitation source, energy-momentum conservation is possible, and the electron can gain or lose light quanta ([Park et al., 2010](#)).

The probability that an electron gains or loses n quanta of the photon energy $\hbar\omega$ at the corresponding momentum transfer $\hbar q$ is given by an expression of the form

$$P_n = J_n^2(2|\beta|)\delta(\omega - \omega_L), \quad (2.1)$$

where J_n is the n th-order Bessel function of the first kind and β is the coupling coefficient of the electron to the laser-induced near-field distribution E [Liebtrau et al. \(2021\)](#).

$$|\beta(\vec{R}, \omega)| = \frac{e}{\hbar\omega} \left| \int \mathcal{E}_z(\vec{R}, z) \cdot e^{-i\frac{\omega}{v}z} dz \right| \quad (2.2)$$

The coupling constant β is the integral along the electron trajectory, where e is the electron charge and ω the frequency of the incident field. The electron wave vector q is written as $q = \frac{\omega}{v}$ where v is the electron velocity.

Here, we assume that the electron trajectory is along the z -axis, and therefore only consider the z component of the field and integrate along the z direction. The integral term is the Fourier Transform of the electromagnetic field of the z -direction, therefore we get a strong coupling coefficient when the spatial Fourier components provides sufficiently large momenta to overcome the phase mismatch between the electron field and the optical pump field in free space. The phase term of [Equation 2.2](#) depends on the electron velocity, so selecting the correct electron velocity is crucial to ensure phase-matching and to produce high coupling coefficients.

We can calculate how the coupling coefficient β links to the expanded energy spectrum using the Bessel function (Equation 2.1) and an energy spread of 0.9 eV, which is a realistic assumption for our system (Solà Garcia, 2021, Chapter 2). For our first tests, we want to ensure that there are considerable side-bands and therefore calculate and plot energy spectra for small β values in Figure 2.1. From this graph we can see that a β value of larger than 0.4 is needed to measure pronounced PINEM side-bands which tend to become more clear with higher β . PINEM can be a highly efficient process for large incident fields, where almost every electron undergoes an energy-gain or energy-loss transition Feist et al. (2015), which can lead to hundreds of energy exchanges Kfir et al. (2020); Dahan et al. (2020). When an electron undergoes several energy exchanges while it passes through the near-field, it might end up with its initial energy if the gains and losses cancel each other out.

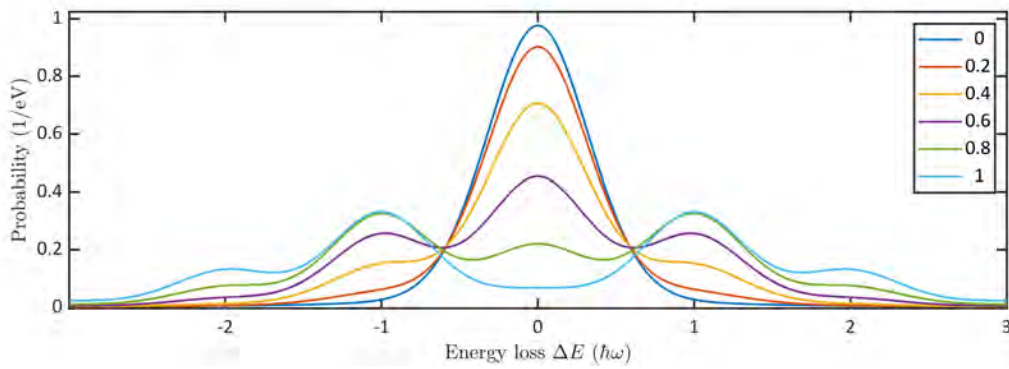


Figure 2.1: Simulated PINEM spectra for betas from 0 to 1 inserted into the Bessel function (Equation 2.1) with an energy spread of 0.9 eV FWHM.

2.2 Nanostructures

PINEM has been observed in structures like needles and nanotubes (Barwick et al., 2009; Feist et al., 2015; Shiloh et al., 2021) or a simple planar silver mirror (Vanacore et al., 2018). A mirror can be used for high-energy electrons, which can pass through the structure, however low-energy electrons in our setup would get stuck in the mirror. Wang et al. (2020) used a photonic crystal consisting of a nanohole array, which allows the electrons to pass through the holes where they can also interact with the near-fields. For our initial tests, these nanohole arrays were used.

The 200 nm thin Silicon Nitride samples were obtained from Tedpella (PELCO Holey Silicon Nitride Support Film for TEM) and have a single window of $450 \mu\text{m} \times 450 \mu\text{m}$ in the middle. We want to simulate these system to evaluate their suitability for PINEM experiments. To do this, the following samples were produced and simulated: A dielectric sample, consisting of only the 200 nm thick Silicon Nitride hole array, and a plasmonic sample, also a hole array on which we evaporated a 75 nm thick gold layer on both sides.

Pitch [nm]	Hole size [nm]	Type	mounting angle [deg]
1000	500	Dielectric	20
400	200	Plasmonic 4 nm Cr and 75 nm Au on both sides	15

Table 2.1: Parameters of the two samples

2.3 Simulation setup

Lumerical FDTD was used to solve the electromagnetic fields of the nanosstructure illuminated by light, and Python to calculate the coupling coefficient beta for an electron trajectory. As can be seen in Equation 2.2, β depends on the integral of the field along the trajectory and the phase term, which is dependent on electron velocity.

In order to simplify the system, we use a plane wave excitation at 1064nm assuming normal incidence. A unit cell which can be seen in Figure 2.2 was defined and symmetric/anti-symmetric boundary conditions were applied. Convergence tests were run to optimize mesh settings (3nm) and ensure the simulations terminate within the simulation time.

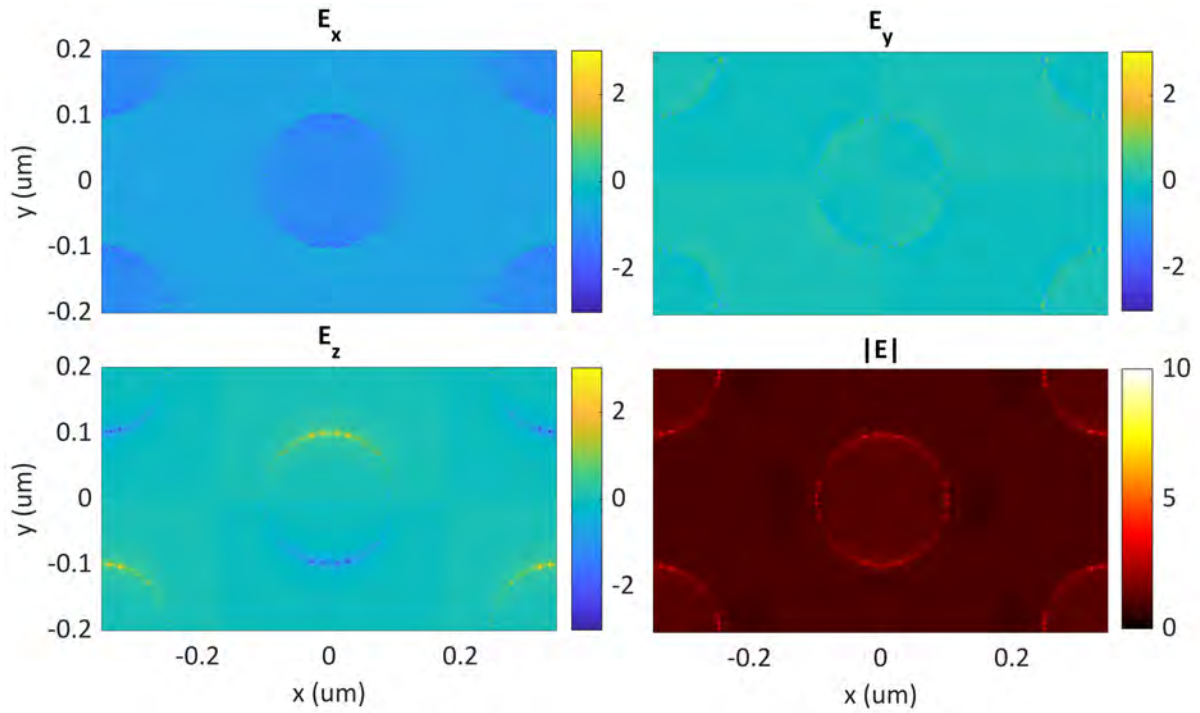


Figure 2.2: Unit cell of the plasmonic sample with simulated field at the top surface, real parts of the E_x , E_y , E_z components and field magnitude.

The field distributions on top of a plasmonic membrane excited with a plane wave source of perpendicular incidence, polarized in y-direction is shown in Figure 2.2. For the PINEM effect, only field components in the z-direction are relevant. High values in the z-direction are located very close to the edge of the hole, and only along the direction of polarization of the source, while in-plane components, in particular the E_x components are present in the entire hole. In order to get high field intensities, accessing these in-plane fields is desirable and can be done by simply tilting the sample, as shown by Wang et al. (2020).

Fields in Lumerical are normalized to 1V/m and were scaled by the approximate excitation field strength that we reach in experiments. In our system, the laser is coupled into the microscope and onto the sample with a half-parabolic mirror, therefore we assume that only half to one-third of the laser intensity reaches the sample.

As a first approximation, we assumed we can reach similar field intensities as [Feist et al. \(2015\)](#), even though our setup and laser source are very different. In our setup, this is 1000 ps laser pulse length, 1 kHz repetition rate, 3 mW power, 5 μm spot size. Later, in experiments which can be seen in [Figure 4.7](#), we realised that these powers cannot be reached without damaging the sample, and therefore recalculated the results with optical field intensities that were achieved just below the damage threshold of our samples (800 ps laser pulse length, 25 kHz repetition rate, 2 mW power, 7.5 μm spot size).

2.4 Results

Coupling coefficients for a 5 keV electron were calculated from the numerically calculated fields, scaled by the excitation field strength for an electron passing close by the edge (at 20 μm distance) of a hole in the plasmonic sample. A cross-cut of the evanescent fields through the hole of this membrane and the electron trajectory can be seen in the top panel of [Figure 2.3](#). Two β values were calculated, once for the initial assumptions corresponding to the field intensities used by [Feist et al. \(2015\)](#), and once for the experimental field intensities that we were able to apply. For the first case, we calculate a β of 1.9479, for the second case β is only 0.2371. In the middle panel, we show the transmitted electrons (or normalized current) as a function of the retarding potential, which acts as an energy filter (see [section 3.1](#)). The derivative of this measurement is the PINEM spectrum, which is plotted in the lowest panel, for both coupling coefficients in comparison with the zero-loss peak ($\beta=0$).

As we see in [Figure 2.3](#), it should be possible to measure PINEM in our experimental setup if high enough field intensities are reached, as the side-bands with a β of 1.9479 can be clearly seen. However, for the a β of 0.2371, which was calculated with the field intensities below the sample damage threshold, the spectrum produces an indiscernible dip with regards to the case where no PINEM happens ($\beta = 0$).

Given the current experimental limitations and the resulting low β values, measuring PINEM is very hard, in particular as the calculations in [Figure 2.3](#) assume that the focus of the electron is a infinitely thin line and can be positions very close to the edge of the hole. In the experiment, this is not the case. The system might drift when switching from a continuous beam to pulsed beam, or during the measurement. To understand how this affects the coupling coefficient β , PINEM spectra of trajectories at different locations from the edge of the hole are plotted in [Figure 2.4](#), using the initial assumptions for the field intensities. We see that even under these favourable assumptions, clear side-bands only emerge when the system is probed close to the edge of the nanohole.

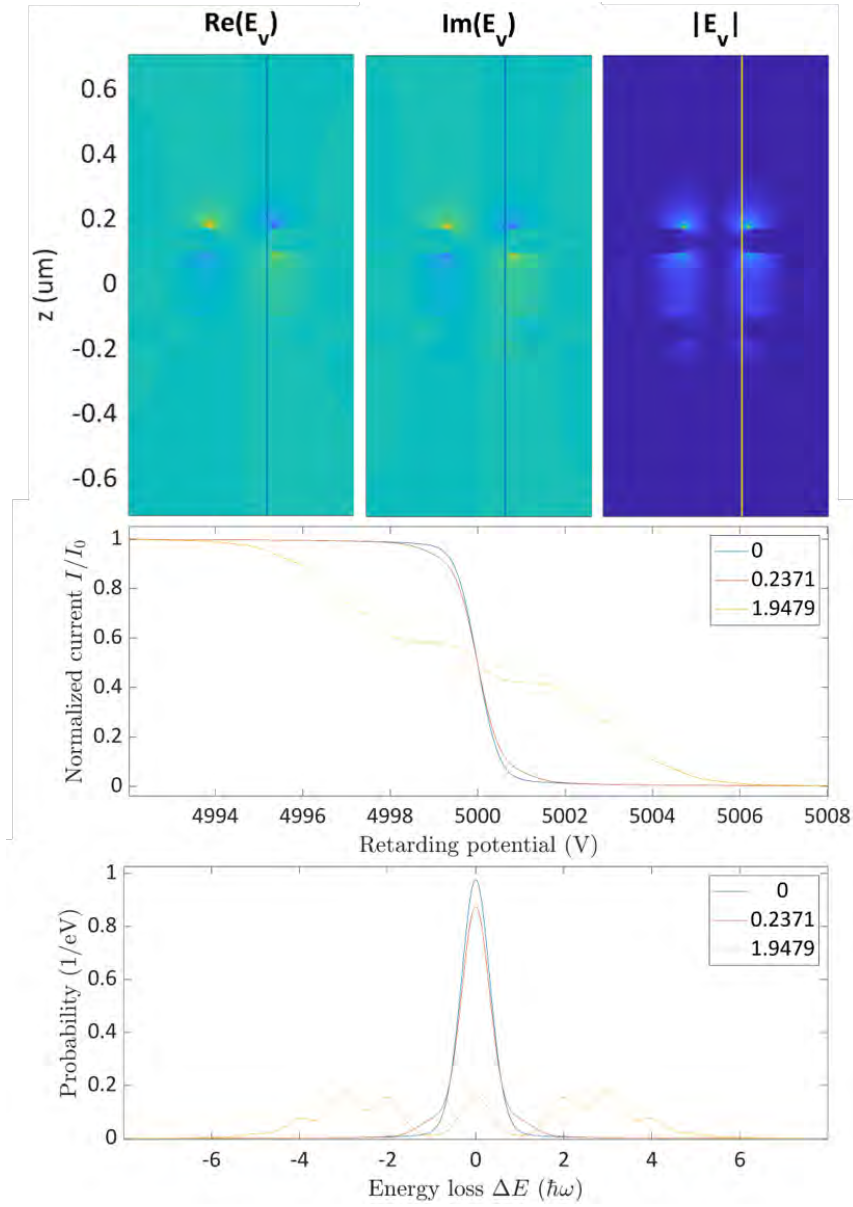


Figure 2.3: Electron trajectories and expected PINEM energy spectra of the Plasmonic membrane for a β of 0, 0.2371 and 1.9479.

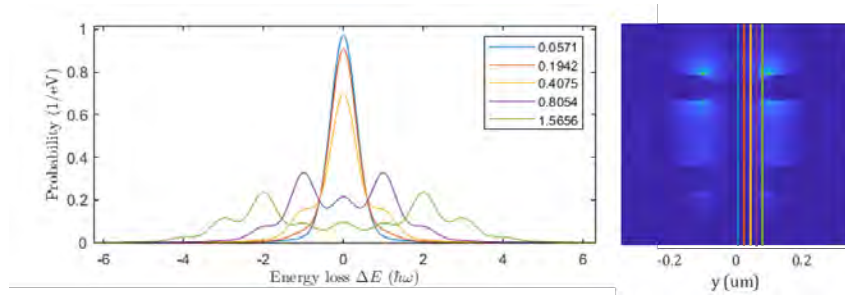


Figure 2.4: Simulated PINEM spectra of electron trajectories at different distances from the edge of the hole.

2.5 Interaction for different electron energies

The impact of the electron velocity on the coupling is illustrated in Figure 2.5, where the squared electron-photon coupling coefficient β^2 is plotted for electron energies from 1 keV to 200 keV and for different electron trajectories along the z direction at different locations within the hole. In the top row, we see results for a holey membrane with 400nm pitch and a hole diameter of 200nm, on the left only 200nm thick Silicon Nitride, and on the right covered with 75 nm of Gold on both sides.

We can see that the coupling is strongest close to the edge of the hole and decays to zero in the middle. Field components with small q extend further into the hole, to which fast electrons with small wave vectors can couple, which explains why the interaction region is wider for high-energy electrons. For electrons with energies of less than 2 keV, oscillations can be seen, which indicate that these electrons fulfil (or don't fulfil) the phase-matching condition, which causes these oscillations.

For our experiments, we chose the top right and bottom left configurations. While these simulations assume that the electron trajectory is perpendicular to the sample surface, the paper by Wang et al. (2020) used the same samples in a tilted position, and a tuneable laser source which allowed to couple to resonances, which significantly increased coupling coefficients. This occurs, because the excited modes predominantly have an in-plane component, which is partly along the electron trajectory when the sample is tilted and can enhance the interaction.

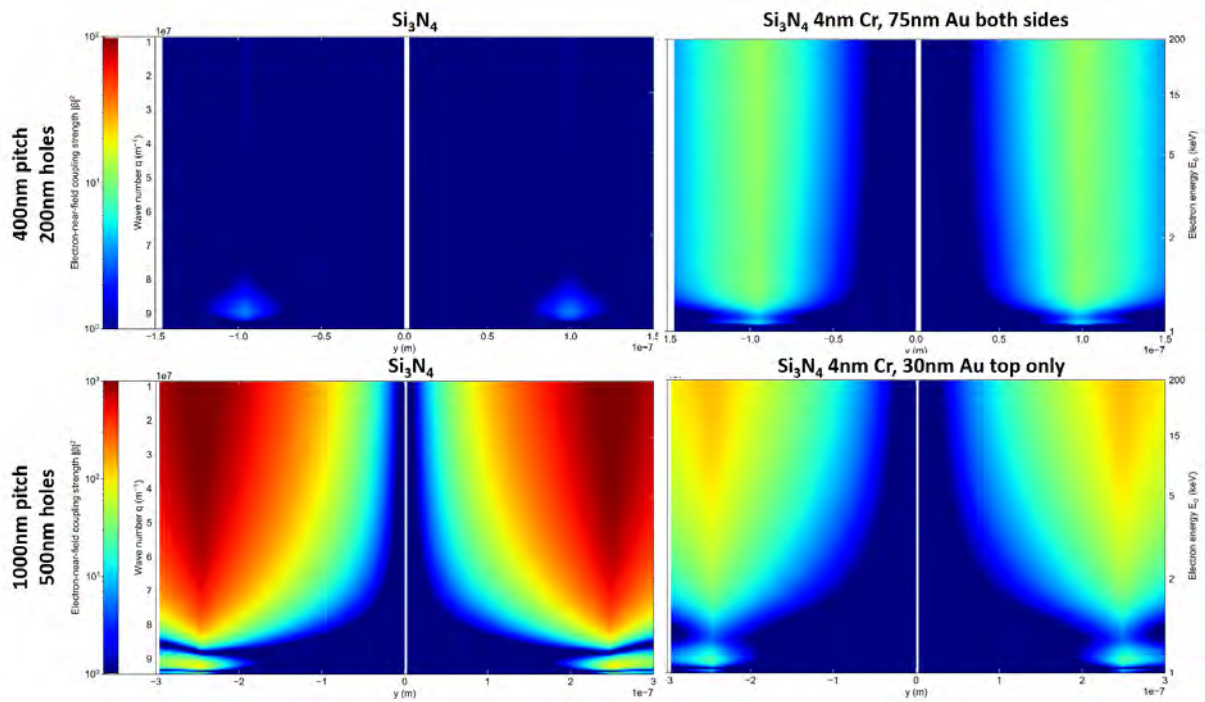


Figure 2.5: Beta squared for two membranes, only Si_3N_4 on the left and combined with gold layers on the right.

Chapter 3

Detector Development

To measure the side-bands of the PINEM spectrum, a measurement device with sufficient energy resolution is required. The laser in our experimental setup emits at a wavelength of 1064nm, corresponding to a PINEM side-band spacing by a photon energy of 1.2eV. We will determine the energy resolution of our setup to resolve these side-bands.

The experimental energy resolution in the detection of these side-bands is limited by two main sources: First, the energy spread of the incoming electron beam, caused by a thermal distribution in the Schottky field emission tip, and second, the intrinsic energy spread of the Retarding Field Analyzer. In previous work, the former has been found to be below 1eV ([Solà Garcia, 2021](#)) and the second 150meV ([van der Heijden, 2011](#)). Thus, it is important that the detection unit does not introduce considerable additional broadening in order to still be capable of resolving the PINEM side-bands.

3.1 Energy Analyzer

The Retarding Field Analyzer we are using was designed at TU Delft in the Thesis of [van der Heijden \(2011\)](#), using the design parameters of [Simpson \(1961\)](#). It was designed to measure the energy spread of a ion source with a highly divergent beam and should be operated at 5kV. However, we want to use it for a tightly focussed electron beam at different voltages. Furthermore, we introduce extensive modifications to the device by adding a deflection unit, a device that blocks light and deflects the electrons, guiding them to the detector ([subsection 3.3.1](#)). This deflection unit introduces further high-voltage elements in close proximity of the system as it was used in Delft. Therefore, simulations of the energy spread of the entire device, and at different operating voltages were performed.

The RFA is also known as filter lens, as it can be used to discriminate against low energy electrons ([Simpson, 1961](#)). It consists of two cathode lenses, placed back-to-back: The first decelerates the electrons and the second re-accelerates them. These lenses also focus the beam into the retarding plane, where the retarding electrode sits, which has a small aperture. Increasing the voltage of this retarding electrode builds up a Coulomb barrier, which prevents electrons with lower energies to pass through. Changing this voltage and repeating the measurement enables the energy analysis. To illustrate the mechanism, simulation results in the cross-cut of the aperture in the scanning electrode are shown in [Figure 3.1](#) a, b and c.

As the voltage at the scanning electrode is increased, we can observe the equipotential lines close to the hole of the scanning electrode. In the case of a, the scanning voltage is below that of the electron beam, so all electrons can pass. In b, the Coulomb barrier is closing, and only electrons at the centre can pass, while the rest is reflected. When the voltage is increased further (c), all electrons are repelled. To measure an energy spectrum, multiple simulations with different applied voltages at the scanning electrode are recorded, and for each measurement, the number of transmitted electrons is recorded.

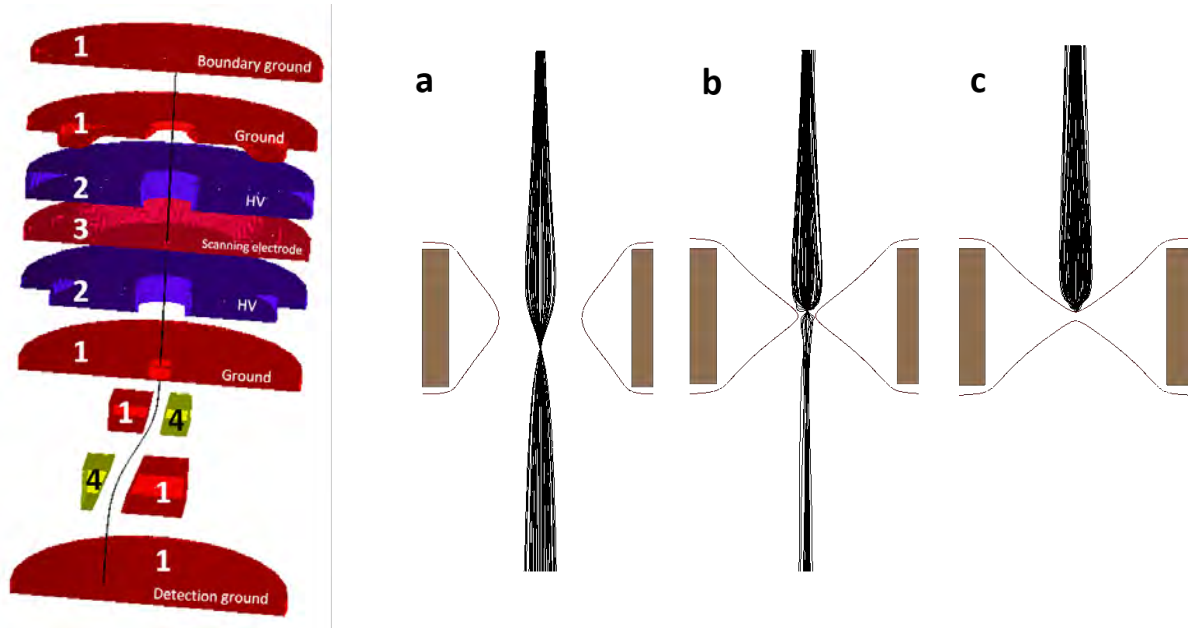


Figure 3.1: Simulation setup of the RFA and example of equipotential lines at an applied scanning voltage (a) below, (b) very close to and (c) above the electron energy.

SIMION is an ion optics simulation software that allows to calculate trajectories of charged particles in electric and/or magnetic fields. The fields in the simulation are solved by solving the Laplace equation by finite difference methods [Manura and Dahl](#).

We use SIMION to simulate the entire Retarding Field Analyzer and deflection unit and determine their combined energy resolution. In order to keep the simulation as close as possible to the real device, all parts of the device were constructed in the CAD (Computer-aided design) software Siemens NX12 and put together in an assembly. From this assembly, the relevant High-Voltage components were cropped and exported as .std files, which were then imported in SIMION.

The linearity of the Laplace equation allows to quickly determine the solutions from linear combinations of individual electrode solutions when the voltage of an electrode is changed. Therefore, the RFA was split up into groups of elements at the same applied voltage. Each of these groups is converted into a 'fast adjust array', which stores the potential at every point on a rectangular grid. It is important that each of the files has the same coordinate system, so that they have the correct relation with respect to one another when they are superimposed, which can be seen in the image in [Figure 3.1](#) on the left side. The numbers correspond to the following groups:

1. Ground: The ground electrodes, and ground elements in the deflection unit plus ground elements at the beginning of the simulation domain and at the end. These ground

elements are required to ensure that the boundary conditions (ground at the pole piece and at the detector) are satisfied in the simulations. Running the simulations without these ground plates results in incorrect results, as the field lines of the simulation are truncated at the border of the electrode.

2. High Voltage electrodes: They are used to create strong field gradients that can decelerate/accelerate electrons and also focus the beam in the retarding electrode.
3. Scanning electrode: The applied voltage of the scanning electrode is scanned during the simulation. The number of this electrode is inserted into the script that performs the sweeps (see [section D.2](#)). In experiments, the scanning voltage is applied on top of the high voltage of the previously described electrodes.
4. Deflection electrodes: These electrodes are set to 1/3 of the High-Voltage. The results of the deflection unit can be seen in [Figure 3.13](#).

Once the geometry and the voltages are set, the electrons are defined. The simulated electrons start from a single point in the center of the system, just underneath the sample, which is represented by a $200\text{ }\mu\text{m}$ thick electrode at ground level. The half opening angle of the diverging beam was approximated as 0.143 degrees, which is the maximum half opening angle that we can expect from the final aperture with a diameter of $70\text{ }\mu\text{m}$, which is used to chop the beam, and is located 14mm above the sample, where the electron beam is focussed.

We can also select the energy distribution of the incoming electrons. We did simulations for two different energy distributions: In the first, electrons have exactly the same energy, in the second, electron energies are described by a gaussian distribution around the initial energy and a FWHM of 0.8eV. An example of the behaviour of these two different simulation scenarios can be seen in [Figure 3.2](#).

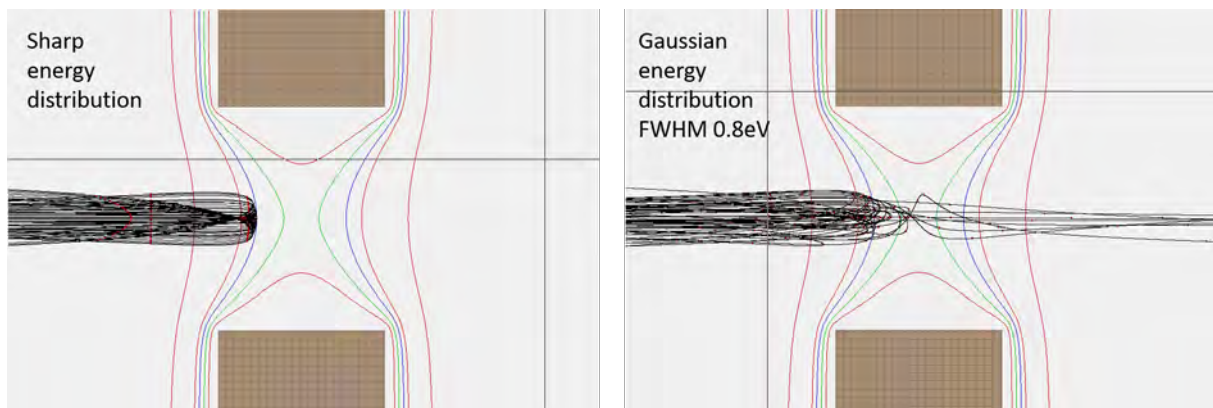


Figure 3.2: Sharp vs gaussian distribution of initial electrons at the scanning electrode.

To calculate the energy spread, 300 simulations of 100 electrons each¹ were performed in SIMION. The data for each electron at its starting point and end point is collected and exported into a .txt file. Then, the number of electrons that were transmitted during each of the simulations is calculated and plotted in Python. In [Figure 3.3](#), we show the results for the

¹Control simulations with up to 10.000 electrons per run were also run, however, 100 electrons were found to provide sufficient information to reliably calculate the energy spread and use much less computing and storage resources.

device operated at 4kV, 5kV and 6kV, where each of the dots represents one simulation result. For a perfect system, and electrons that have the same energy, we expect a step function. However, it is important to keep in mind that the barrier in the RFA does not measure the total kinetic energy, but the momentum perpendicular to the equipotential lines [Simpson \(1961\)](#). Due to the geometry of the hole, these potential lines are not straight, and electrons arrive at slightly different positions and with different angles at the equipotential lines, which can be seen in [Figure 3.2](#). These two geometric factors cause the intrinsic energy resolution (blue dots).

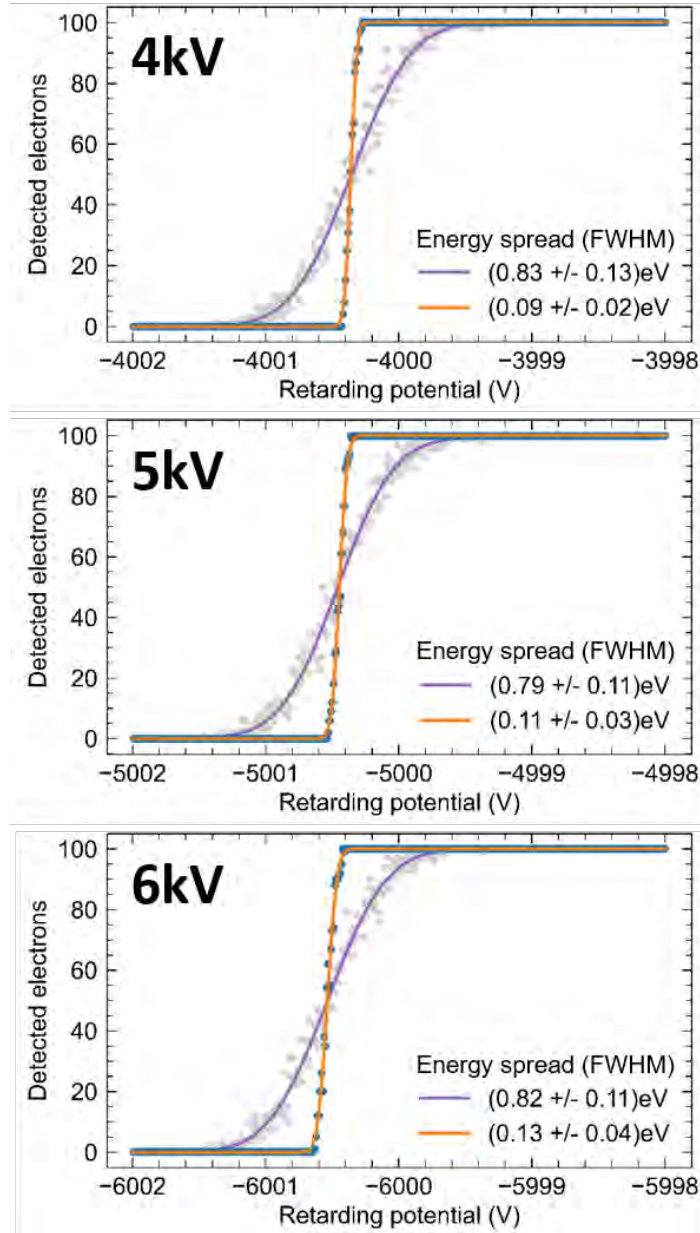


Figure 3.3: Intrinsic energy resolution (blue and orange fit) and combined with incoming electrons with a Gaussian distribution of 0.8eV (grey and violet fit) of the entire system operated at 4, 5 and 6keV.

The second set of data in [Figure 3.2](#) show the simulation results for an incoming electron beam with a gaussian energy spread of FWHM 0.8eV (grey dots), a realistic assumption for our setup ([Solà Garcia, 2021](#)).

To get a numerical value for the energy spread, the data is fitted with a pseudo-Voigt function to determine the energy spread

$$PV_{CDF} = k \cdot \left(-\frac{A}{\pi} \cdot \arctan\left(\frac{x - x_0}{w}\right) + \frac{A}{2} \right) + (1 - k) \cdot \frac{A}{2} \cdot \left(1 - \operatorname{erf}\left(\sqrt{\log(2)} \cdot \frac{x - x_0}{w}\right) \right) \quad (3.1)$$

with k the fraction that the Lorentzian contributes and w the half the FWHM of the corresponding PDF. These fits can be seen as the orange and violet lines in [Figure 3.3](#).

The intrinsic energy spread is around 0.1eV for all three energies, which does not only confirm that the addition of the deflection unit does not decrease the performance of the device, but also that it can be operated in the entire range of 4kV to 6kV. We also learn that the intrinsic energy spread is small compared to the thermal spread of the microscope, which dominates the energy spread. Furthermore, as all simulations were performed with the simulated deflection unit, we find that it does not deteriorate the energy resolution, and confirm that none of the electrons that are transmitted through the RFA get lost in the deflection unit.

In the previous simulations, the incoming electron beam entered the RFA exactly in the centre above the scanning aperture. In experiments, there might be an offset, as there is no possibility to align the sample independently from the detector. This means the electron beam can enter the system off-centre, with negative consequences on the energy resolution as was further studied in simulations. The further the electron beam moves away from the centre, the worse the energy resolution. In [Figure 3.4](#) we can see that there is a radius of around 20-30 μm within which the energy resolution is still very good. We find further, that for larger offsets some of the electrons are never transmitted, even though the scanning voltage is below the energy, which significantly decreases the signal and increases the noise from scattered electrons, leading to a worse energy resolution. These simulation results are confirmed by experimental data, where an aperture of a similar size is visible just below the voltage when all electrons are repelled (see [Figure 4.1](#)).

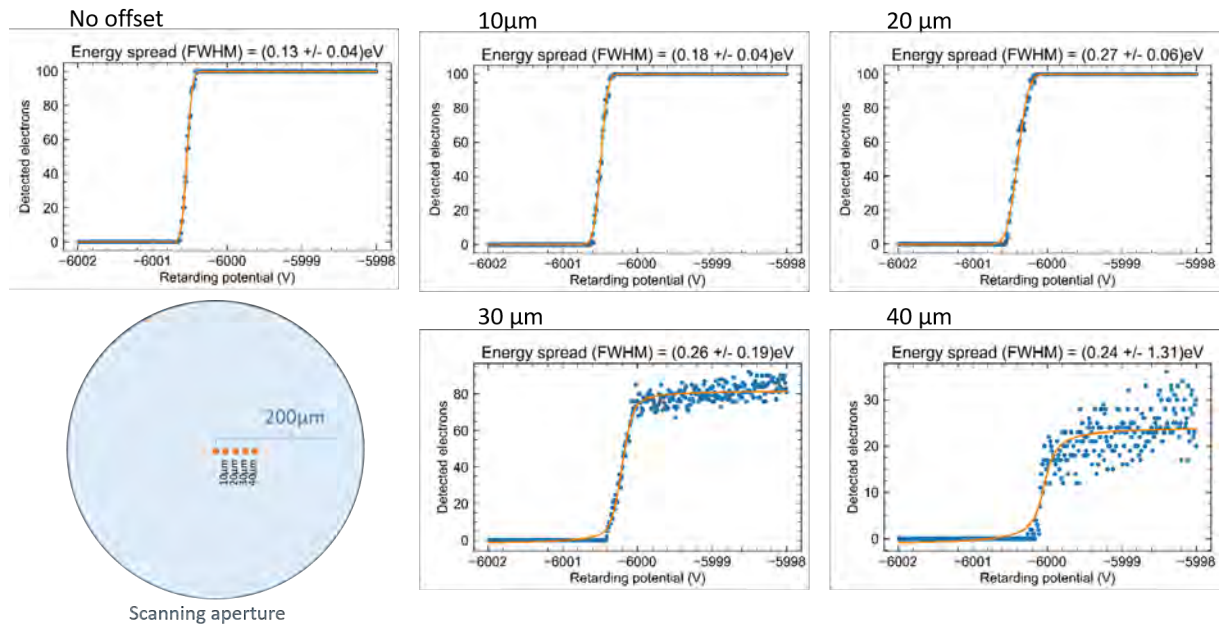


Figure 3.4: Energy resolution of a sharp 6keV electron beam at starting locations from the centre.

3.2 MiniPix Detector

After the energy analysis in the RFA, a sensitive detector is needed to detect and count how many electrons have passed through the energy filter at each voltage step. In the setup developed by [van der Heijden \(2011\)](#), this was done with a Faraday cup, which reached sensitivities down to a few tens of femtoamps. This is not enough for our experiments, where we need to detect electrons in the attoampere range.

To this end, we introduced the single-electron detector MiniPix by Advacam with a Timepix3 chip ([Appendix C](#)) into our measurement setup in order to improve sensitivity and consequently significantly decrease integration time compared to the Faraday cup, that was previously used. This detector is built for high-energy X-ray photons and normally has an Aluminium layer on top of the highly-doped Silicon p-n junction, which prevents lower-energy particles and photons to be detected. In order to detect low-energy electrons, which would get stuck in such a layer, we ordered the detector without the Aluminium layer. This enables us to detect electrons with energies as low as 5 keV, even if the detection efficiency is much lower than for higher electron energies. In [Figure 3.5](#) we see the number of detected electrons at 5, 10 and 30 keV with different threshold voltages, an internal parameter that can be used to reduce noise by cutting off low-energy events. The coloured data points were acquired when the electron beam is on, the black data points are the background. At 30 keV ([Figure 3.5](#)), we see that the signal-to-noise ratio (the number of electrons that is detected with respect to the background) is always good. For the measurements of 10 and 5 keV, on the other hand, the signal-to-noise ratio is very low. We also observed worse performance of the detector when it heated up. The temperature of the detector was increasing during the measurements, and as we started with 30 keV, then measured at 10 keV and finally at 5 keV, we decided to build a cooling system to stabilize measurements.

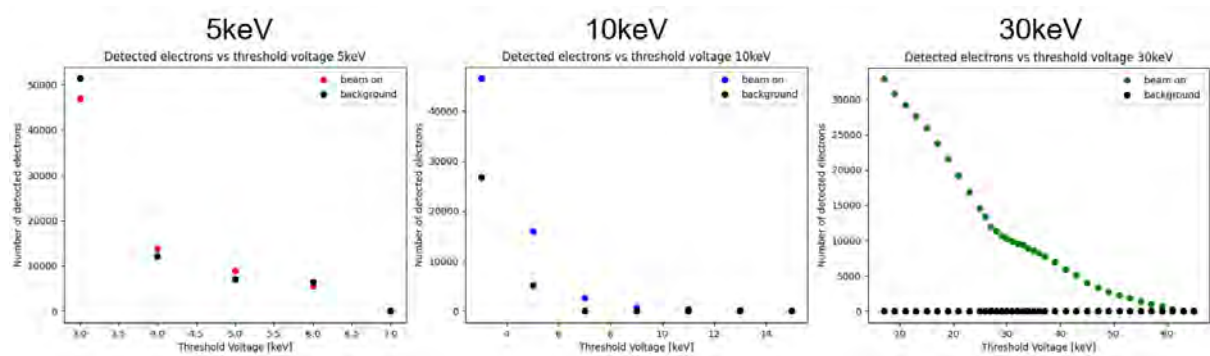


Figure 3.5: Threshold sweeps of MiniPix at different electron energy settings at high sensor temperatures (around 50 degrees Celsius).

The detector is not designed to be used in vacuum. We found that it can be operated in vacuum, but it requires active cooling. The analogue-to-digital conversion and read-out process is happening inside the detector, and the data can be transmitted digitally via a USB interface and connected to a computer via an adapted feedthrough in the microscope. This needs energy (power dissipation of 2.5W). In vacuum, the device cannot be cooled by convection, which causes the detector to heat up. The temperature range the detector should be operated with is 20-30 degrees Celsius, as higher temperatures could damage the solder connections and

make the detector unusable. Measurements at high, and unstable temperatures (Figure 3.5)² showed that the background signal (measurement without the electron beam) was stronger than the signal of the electrons, in particular for low electron energies. The built-in detection threshold function could not eliminate this problem, therefore, a cooling system had to be built.

Through the internal thermometer, the temperature of the detector can be monitored in the Pixet Pro software. The cooling system uses copper strands, clamped to the long side of the detector by aluminium blocks, which are fixed to the ground plate with screws (Figure 3.6). The copper strands are then connected to the cryogenic stage of the microscope, which is cooled by flowing nitrogen that passes through a spiral heat exchanger which is inserted into a dewar of liquid nitrogen.

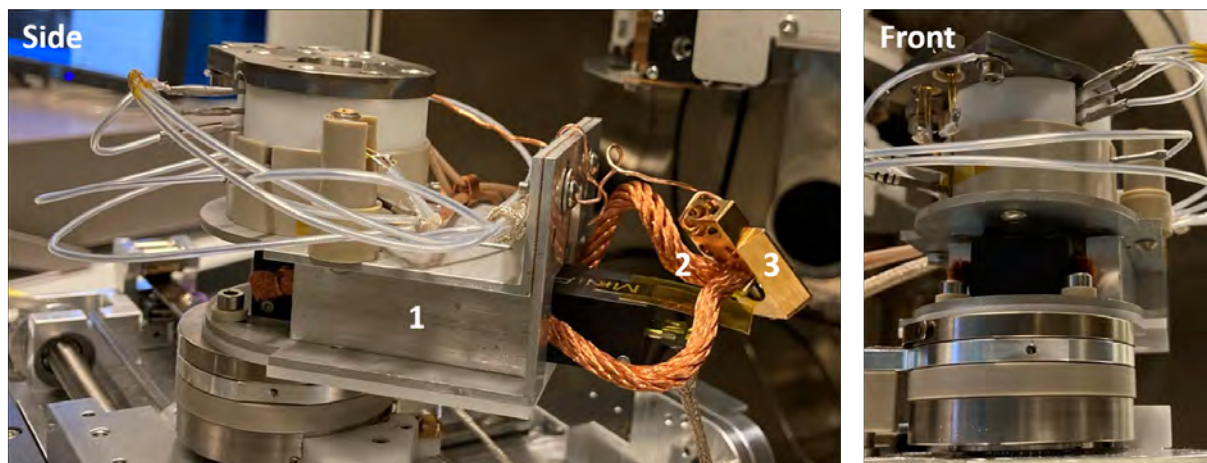


Figure 3.6: Cooling mechanism for the MiniPix detector with (1) Aluminium blocks, (2) copper strands and (3) the connector boat to the cryostage.

With this simple cooling system, the detector can be kept at a constant temperature of 27 to 28 degree Celsius for long times, which lies within the optimal operating temperature and eliminates background noise.

²Settings: SEM: Spot 2, C2= 0,1783 (5keV, Ct=6000); 0.3088 (10keV); 0.4765 (30keV). Aperture 7, Blanker1, square wave, (-5V to +5V, f=1MHz); MiniPix: Frames mode, acquisition time 0.001s, 90 counts, Bias 200V

In initial tests, the laser was coupled into the chamber and the signal was measured with the MiniPix detector. Several measurements were taken at different distances from the parabolic mirror [Figure 3.7](#). From these images we see, that the laser is collected through the mirror, and that it can be detected on the MiniPix detector. The wavelength of our laser (1064nm) is within the spectral response of the Si detector. The beam is also strongly divergent, which means that most of the laser light will be blocked out by the small aperture in the scanning electrode when the MiniPix is placed underneath the RFA. In the images further away from the pole piece, we can also see the hole in the mirror in the middle, where no laser light is reflected. The concentric circular features are artifacts from the lenses in the fibre coupling unit.

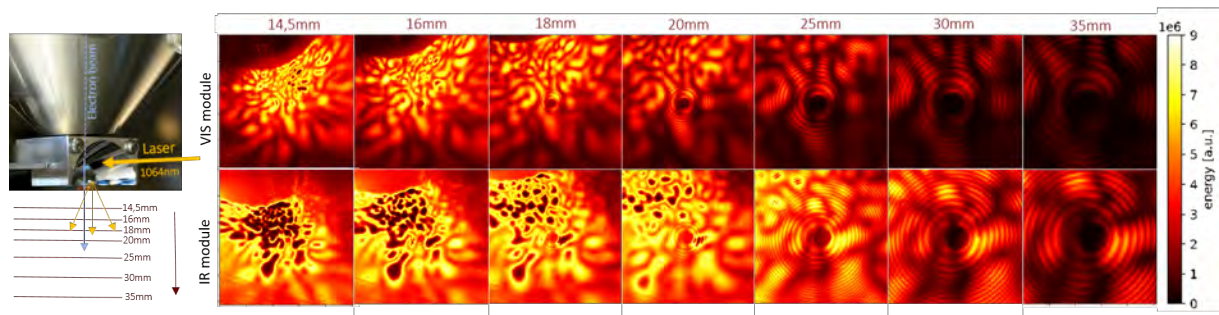


Figure 3.7: Left: Pole piece of the SEM and parabolic mirror which is used to couple in the laser. Right: Laser spot at different heights below the pole piece.

3.3 Deflection Unit

Measuring PINEM in our setup, requires that the laser and the electron beam overlap temporally and spatially. Previously, a Faraday cup that only measures the current induced by charged particles was used in the setup. However, the detection sensitivity was limited to a few tens of fA, which is not sensitive enough due to the very short electron pulses, which have to be synchronised with the laser pulses. To detect PINEM events under our experimental conditions, a new, pixellated Silicon detector (MiniPix) was installed. This is much more sensitive, but detects photons as well as electrons. The laser intensities required to excite the nanostructure are so high that they completely obscure the signal of the electrons on the sensor. At low laser intensities ($100 \mu\text{W}$), the spatial overlap of the signal from the electrons (bright spot) and laser light (large red spot) can be seen in Figure 3.8. We can use a trick in order to circumvent this problem, we use a deflection unit. Electrons are charged particles, so they can be deflected in electric fields, while photons are not affected. Using this difference, we can circumvent this problem by blocking the laser light and bending the beam so only the electrons reach the sensor plane.

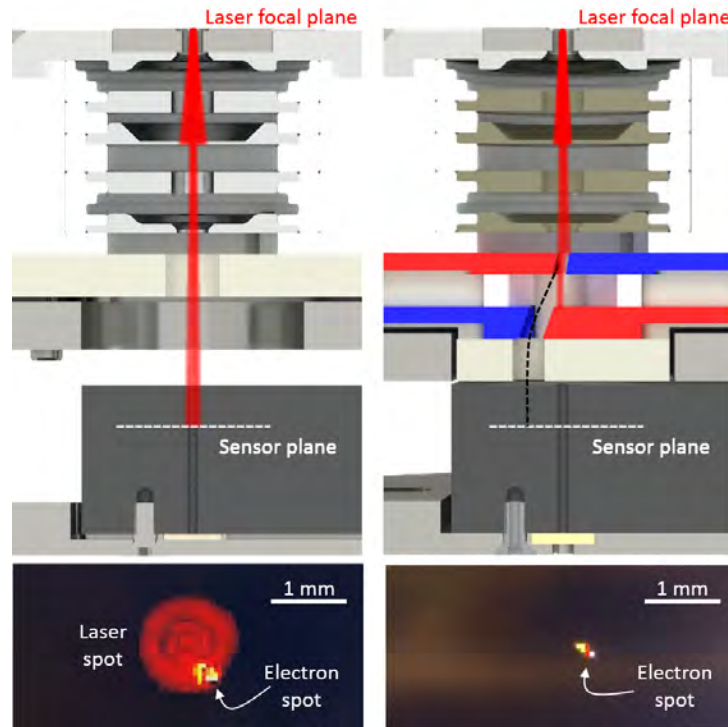


Figure 3.8: Crosscut of the structure without and with the deflection unit.

There are several constraints for the design a deflection unit: Space in the SEM chamber is limited in vertical direction underneath the pole piece of the electron gun, also because we introduce the parabolic mirror for light focussing. In our setup, we can only afford an additional height of 10mm for a deflection unit, so the device has to be extremely compact. A compact design means that electrodes at high voltages (4 - 6 kV³) need to be placed close together, therefore lower voltages are preferred to avoid electrical breakdown. Furthermore, lower voltages at the deflection unit would interfere less with the strong fields at the scanning

³4kV is the minimum electron energy that can be detected with the MiniPix detector, 6kV is the maximum safe voltage that can be applied to the RFA

electrode, which determine the energy resolution. As the detection efficiency of our MiniPix detector is worse at lower electron energies, the deflection unit must not slow the electrons down.

To get a first estimate of the deflection that is achievable within these constraints, a simple analytical parallel plate deflector model was used. We assume that the field is perfectly uniform, and that fringe fields play no role and with the electron trajectory oriented parallel to the deflecting plates. In our system, which is pictured in [Figure 3.9](#), the initial direction of the electron is denoted by z , and the deflection happens in y direction.

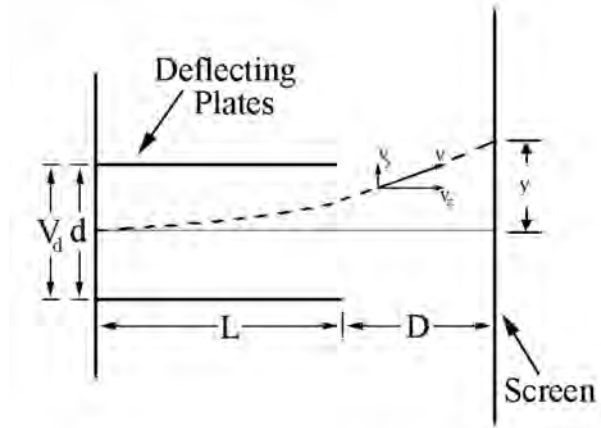


Figure 3.9: Simple model of electron deflection between two parallel plates ([Spaldin, 2012](#))

We assume a constant electrostatic field between two parallel plates. The force an electron with elementary charge e feels in y direction in such a field is

$$F_y = e \cdot E_y \quad (3.2)$$

The strength of the electric field amplitude in direction perpendicular to the surface of the plates is given by

$$E_y = -\frac{dV}{dy} = -\frac{V_d}{d} \quad (3.3)$$

Using Newton's second law and the kinematic relations, the distance in y direction that the electron has been deflected at a distance D after leaving the plates can be calculated as

$$y = \frac{e \cdot E_y \cdot L}{m \cdot v_x^2} \left(D + \frac{L}{2} \right) \quad (3.4)$$

One can then express the electric field using [Equation 3.3](#) as the voltage difference applied to the two deflector plates:

$$y = \frac{V_d \cdot L}{2 \cdot d \cdot V_{acc}} \left(D + \frac{L}{2} \right) \quad (3.5)$$

With this formula, we found a combination of two deflection plates that can achieve a lateral deflection of around 2mm within the vertical distance of 10mm that is available for the device, using only one third of the High-Voltage of the RFA (4, 5, and 6kV). The geometric shadow of the laser is around 1mm in diameter, which should be blocked. The geometry of this first model can be seen in [Figure 3.12](#) and consists of one pair of parallel plates that are 2mm long and 1mm apart, and a second set of slanted plates that are 2.3mm thick and 2mm apart.

3.3.1 Electron Trajectory Calculations

In order to ensure that the electrons will be bent correctly, and will not end up in the deflection electrodes, we need to include the influence of fringe fields and asymmetries. To do this, numerical simulations are required. The programme Maxwell from Ansys Electronics was used to calculate the electrostatic fields of this initial deflection plate geometry in 3D. As it is a Finite Element Method (FEM) programme using triangular meshing, it is crucial to ensure that the meshing is fine enough to resolve the fields, in particular around sharp corners. In order to facilitate the simulations, sharp edges were rounded, and the simulation domain was reduced to the relevant features. Due to translational symmetry (along the x-axis), the problem was reduced to a 2D geometry.

From the simulations ([Figure 3.12](#)) it can be seen that fringe fields do play a significant role, and that fields are not homogenously distributed within the slits, as it was assumed in the simple parallel plate model. We wrote an electron trajectory programme in Python to calculate and visualize the path of electrons in the deflection unit.

Similarly to the case of the two parallel plates with a potential difference, the force acting on the electron is given by

$$\vec{F} = e \cdot \vec{E} \quad (3.6)$$

The only difference is, that the electrostatic field is now defined locally by the E-field vectors, which were exported from Ansys with a resolution of 0.02mm. As in the previous model, the z -direction is the same as the initial direction of the electron, and the y direction is perpendicular to it (and corresponds to the deflection). The y and z coordinates (step n) as well as the velocity in y and z -direction (last step, $n - 1$) of the electron are used as input. The system is divided into a number of steps in z -direction, for each of which we calculate the following values:

The electric field at the coordinates (of step n) is evaluated, and the force on the particle is calculated for each of the two components

$$F_y = e \cdot E_y \quad F_z = e \cdot E_z \quad (3.7)$$

which are used to obtain the acceleration by dividing by the electron mass

$$a_y = \frac{F_y}{m} \quad a_z = \frac{F_z}{m}. \quad (3.8)$$

To obtain the velocity in this step, we first determine the how long the electron remains within this step of size Δz in z -direction, as $\Delta t = \frac{\Delta z}{v_{z[n-1]}}$. With this, we calculate the displacement as

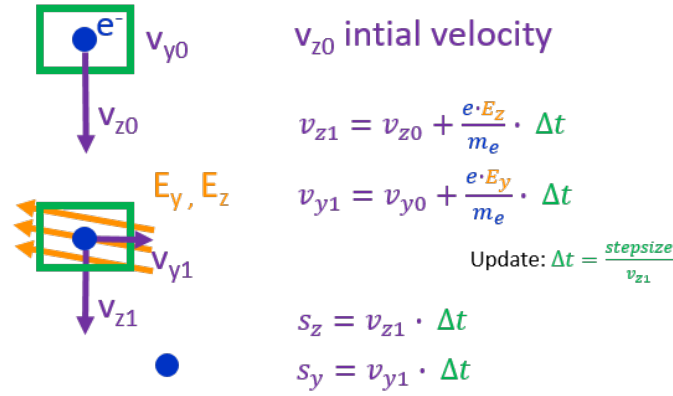


Figure 3.10: Electron trajectories are calculated by adding electron velocities in y and z direction. The external field acts on the particle and accelerates (or decelerates) it in each step. The new spatial coordinate (s_y and s_z) are calculated with the updated velocities and used as input for the next step.

the sum of the velocity in the previous time-step (n-1) and the velocity the particle is acquiring in this time-step (n) with interaction time Δt

$$s_y = \left(v_{y[n-1]} + a_y \cdot \Delta t \right) \cdot \Delta t \quad s_z = \left(v_{z[n-1]} + a_z \cdot \Delta t \right) \cdot \Delta t \quad (3.9)$$

So far, classical mechanics was used to calculate trajectories, which is a valid assumption given that the deflection unit will operate at electron energies on the order of a few keV, which corresponds to only 15% of the speed of light, and a Lorentz factor barely above 1. To ensure the model is complete, we also include relativistic effects into our model. The Lorentz factor γ describes how much time, length and other properties change for a particle while it is moving. It can be defined via the velocity, impulse or energy of an electron.

$$\gamma = \frac{1}{\sqrt{1 - \left(\frac{v}{c}\right)^2}} = \sqrt{1 + \left(\frac{\vec{p}}{m \cdot c}\right)^2} = \frac{E_{kin}}{E_0} + 1 \quad (3.10)$$

As the kinetic energy is calculated for every time-step, the latter expression is used for the programme. The relativistic term for the force is

$$F = \frac{\Delta p}{\Delta t} = \gamma^3 \cdot m \cdot a$$

where $p = \gamma \cdot m_e \cdot v$ which leads to the two formulations for the differential velocity

$$\Delta v_{classical} = \frac{e \cdot E}{m_e} \cdot \Delta t \quad \Delta v_{relativistic} = \frac{e \cdot E}{\gamma^3 \cdot m_e} \cdot \Delta t. \quad (3.11)$$

This can be implemented directly into [Equation 3.7](#) and is updated in each step.

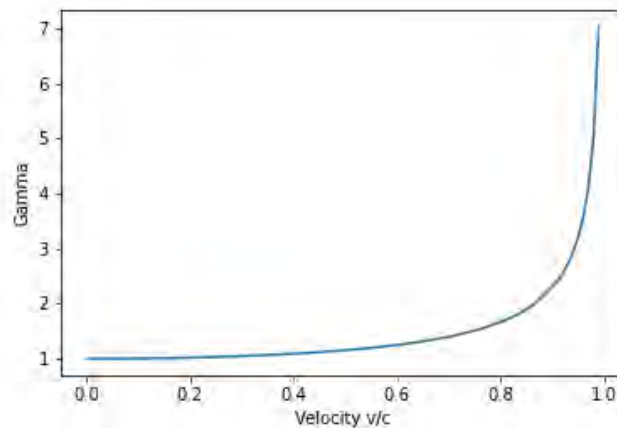


Figure 3.11: Lorentz factor for velocities up to the speed of light c

3.3.2 Simulation Results

Figure 3.12 show the simulation results for 6 keV electrons that we designed with the simple parallel plate model. We see that the electrons would have intersected with the electrodes. The simple model only considers the forces acting on the particle in the field, and therefore electrons seem to fly through the electrodes unaffected.

In an iterative process, the geometry was altered in order to optimize the electron trajectories. Another important parameter that was optimized is the energy they lose while passing through the system. The final geometry and the trajectories can be seen in Figure 3.13. In both results, solid lines represent electron trajectories that were calculated classically, and dashed lines represent relativistic electrons. For the relativistic effects, only very small deviations are observable.

The results obtained with the scripts above were verified by using SIMION at 4, 5 and 6 keV, which is shown in Figure 3.14. We see good agreement between the self-written programme and the commercial software in all three cases, and also the same trajectories for all three energies, which is expected because the electric fields scale linearly.

The final deflection geometry was incorporated into the Retarding field analyzer. New electrodes with the specified dimensions were designed and manufactured from Titanium. Technical drawings for the deflection unit and its parts can be found in Appendix E.

For the next iteration of the deflection unit, an even more compact design with only two electrodes that need to be connected was designed. This has the significant advantage that the unit can be placed closer to the holder, and is more stable internally.

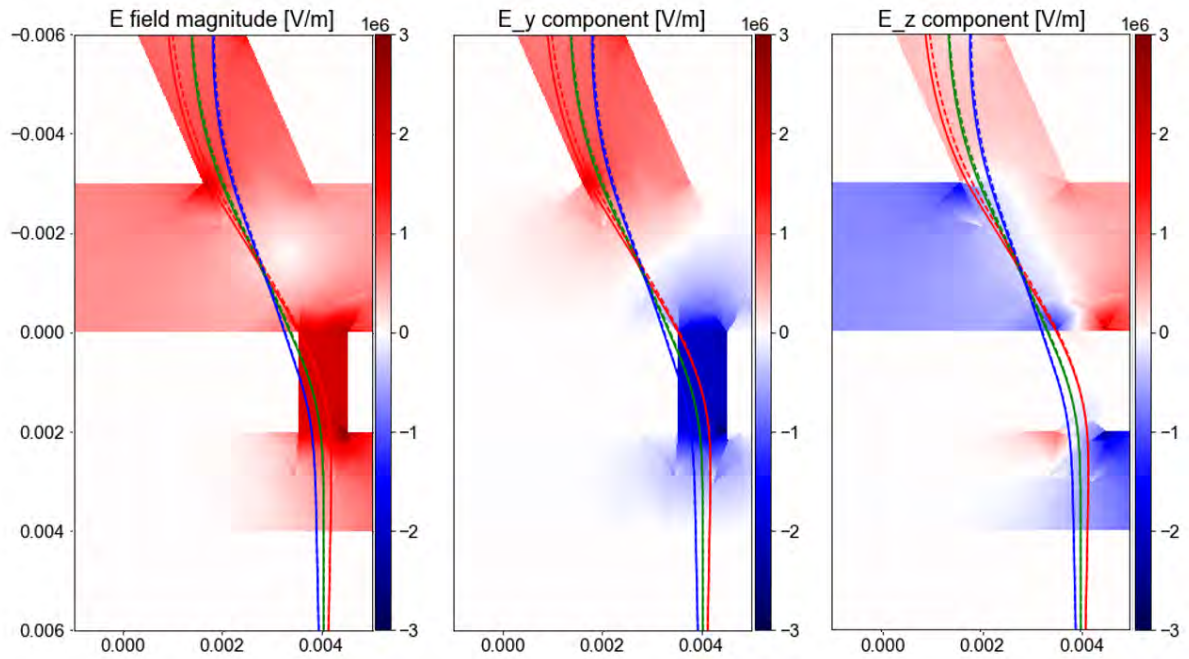


Figure 3.12: Electrostatic field magnitude and components and calculated trajectories for three electrons. Solid lines represent classical particles, dashed lines relativistic electrons. Electrons start at (0.004,+0.006) and move in negative z direction. In the initial geometry, electrons would collide with the electrodes.

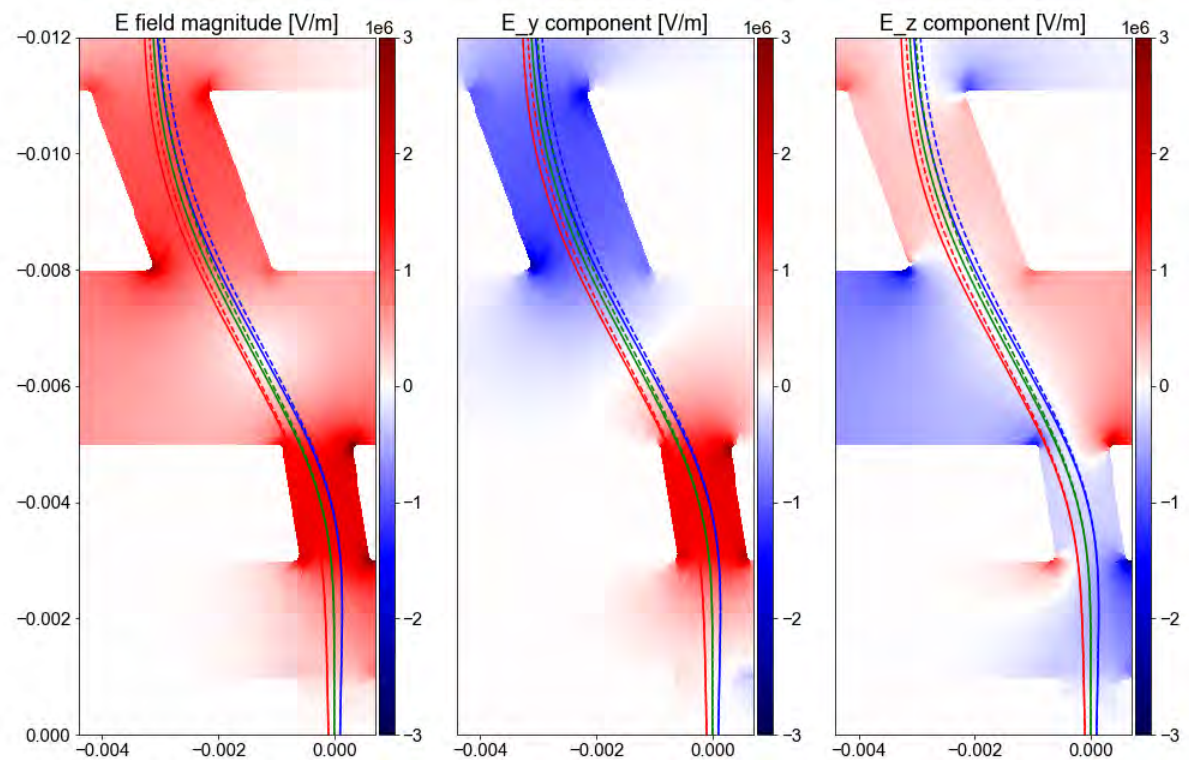


Figure 3.13: Electrostatic field magnitude and components and calculated trajectories for three electrons. Solid lines represent classical particles, dashed lines relativistic electrons. Electrons start at (0,0) and move in negative z direction.

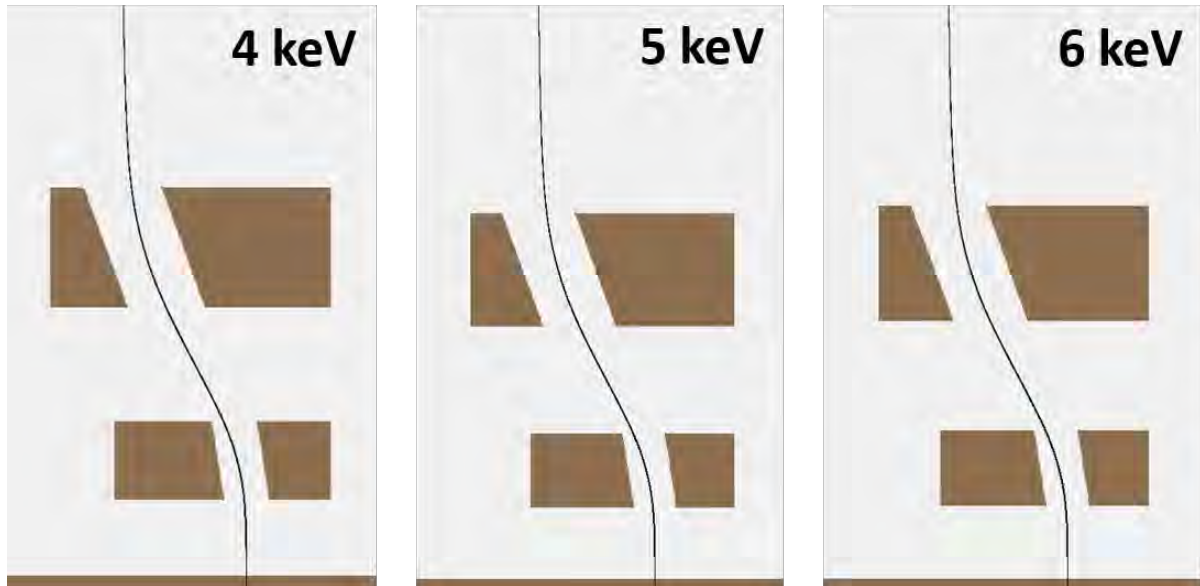


Figure 3.14: Trajectories of 5keV electrons in the deflection unit after they passed the RFA unit.

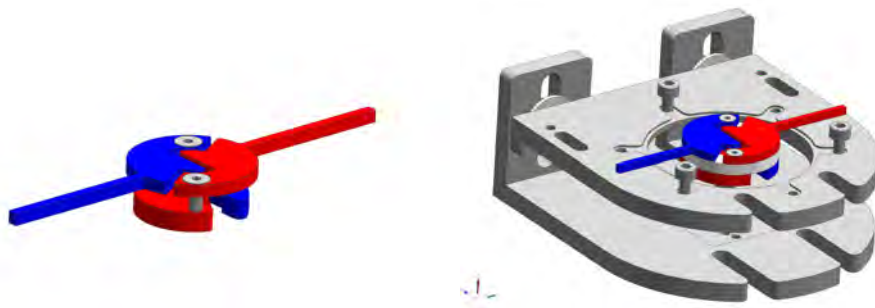


Figure 3.15: The new and more compact design of the deflection unit.

Chapter 4

Results

In this section the RFA, the deflection unit and the entire detection system are tested under experimental conditions for PINEM measurements.

4.1 Retarding Field Analyzer

Applying the high voltage changes the electric field lines and influences the path of the electrons, as predicted in the simulations [Figure 3.1](#). This can be seen in a series of measurements where the RFA is installed without any sample. In [Figure 4.1](#), several images at different voltages are displayed. We look at the top of the RFA, where the large opening is the sample holder, which is on ground potential, and below the retarding electrode with a small aperture. These images are taken with 5 keV electrons, which are affected by electric lenses in a similar way to light in optical lenses. We can see, that the image changes, is distorted and appears to move, similar to effects we know from optical lenses as the voltage is increased. When we arrive in the region of operation (4990 V and upwards), we can see that the hole in the scanning electrode appears a lot smaller than in the initial images (eg. at 250 V). This is the experimental confirmation of the closing up of the equipotential lines, as simulated in [Figure 3.1](#).

At voltages higher than the electron energy (5 keV) eg. 4998 V upwards, all electrons are repelled and a new feature appears in the images. What we see is a reflection of the electron gun, where the electrons come from, so the RFA now acts as a mirror.

When a Silicon Nitride membrane is placed in the sample holder above the RFA, the scanning aperture can still be seen through the membrane, which is convenient to find the location above the aperture. In [Figure 4.2](#), one can see the system at different voltages. At 6000 V, a small square appears, which is the reflection of the membrane from below.

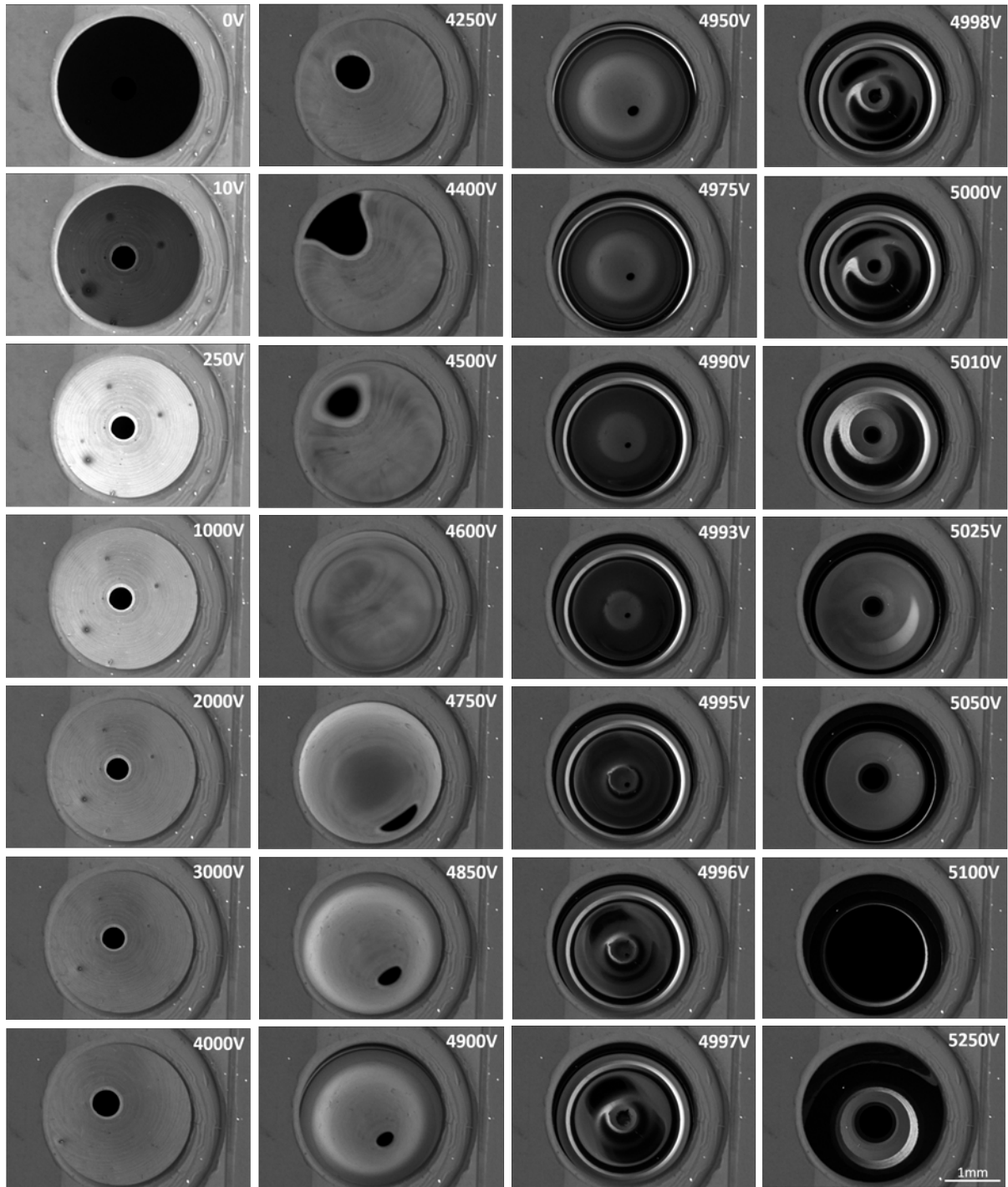


Figure 4.1: RFA imaged in the SEM with 5keV electrons while the voltage of the RFA is gradually increased.

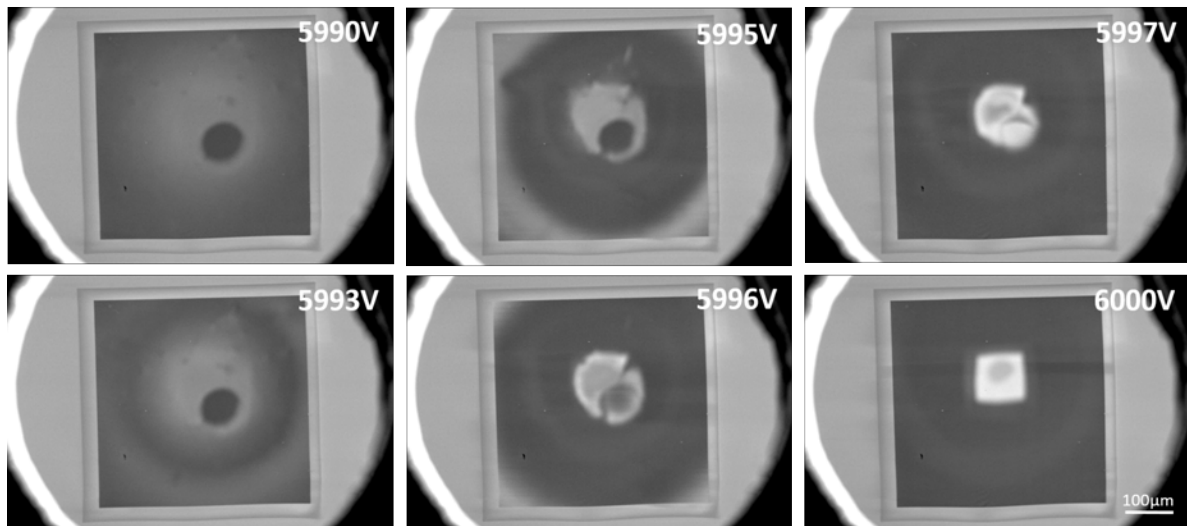


Figure 4.2: RFA seen through 1000 nm pitch 500 nm hole diameters silicon nitride membrane.

4.2 Deflection Unit

The deflection unit was manufactured, assembled and tested with the entire RFA. A potentiometer allows to change the applied voltage at the two deflection electrodes (see [Figure 3.1](#)) from 0 to 50% of the high voltage in the RFA. This enables the user to turn the deflection on and off easily, and allows to use high beam currents and turn the deflection unit off, shielding the detector from potential damage. The unit is designed to operate at 1/3 of the High Voltage, which was confirmed as the optimal voltage in the experiment.

In [Figure 4.3](#) we see this signal on the detector area. At experimental conditions for the PINEM measurements and good alignment of the parabolic mirror, a small signal from the laser light was detected, which is probably due to scattering inside the deflection unit. However, there is no spatial overlap between the electron beam and the scattered laser light, which allows to exclude the affected pixels from the measurement.

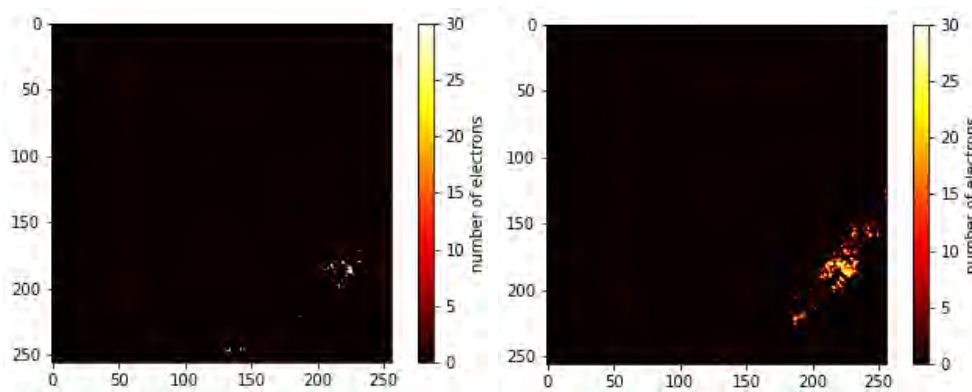


Figure 4.3: Detected signal from the laser. Left: 0.7 mW (1 kHz, 15%) and right: 26.3 mW (25 kHz, 35%).

The deflection unit can be turned on by turning up the voltage on the potentiometer, which can be seen in [Figure 4.4](#). In subfigures a to i, the voltage is gradually increased, and the electron beam (in scanning mode in the SEM) is scanned across the aperture in the retarding electrode and appears as a line-shaped signal on the sensor, which corresponds to the slit formed by the deflection unit. The optimal operating voltage is achieved approximately in subfigure f, corresponding to 1/3 of the high voltage.

These results show that the deflection successfully deflects the laser light and bends the electron beam to a location on the sensor where it can be detected without any signal from stray laser light.

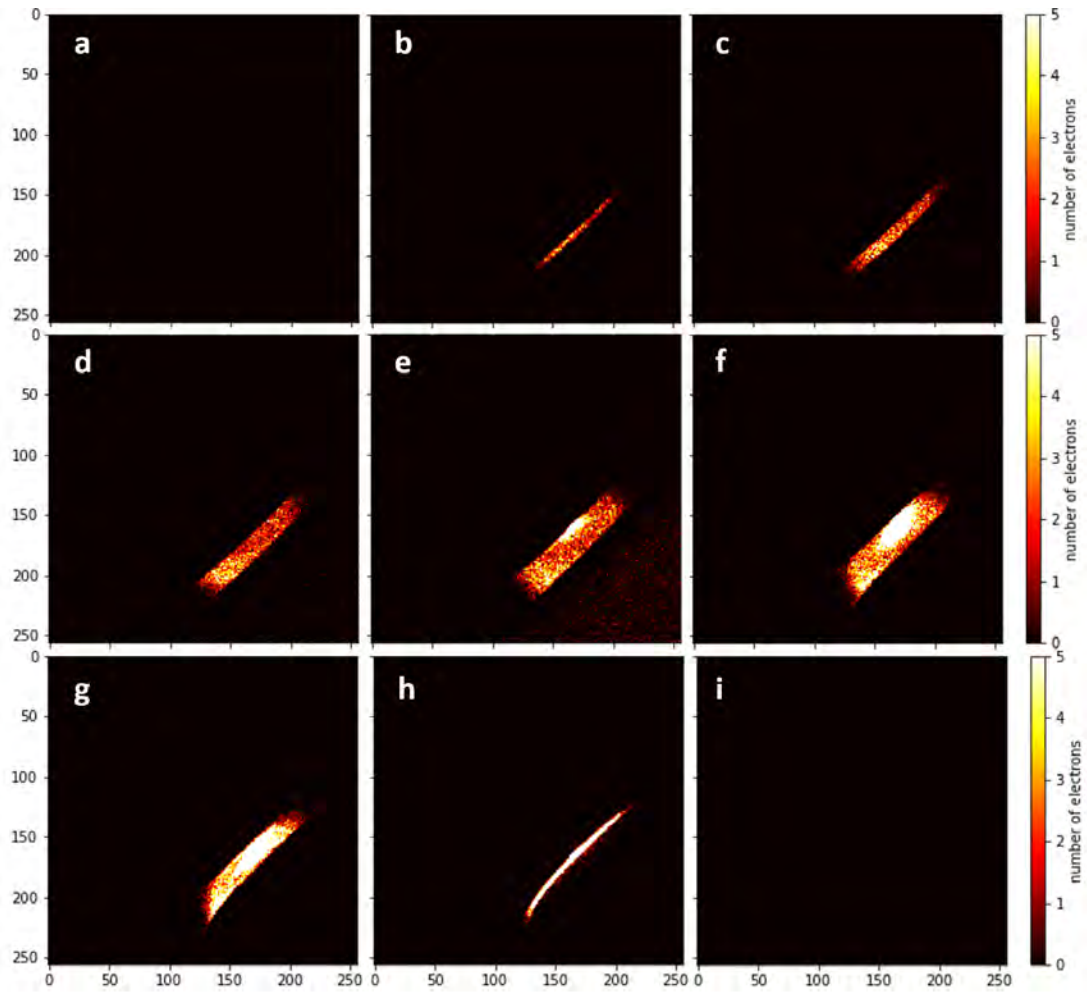


Figure 4.4: Detected signal of a scanning 5 keV electron beam at the sensor for different positions of the potentiometer, going from 0 V (a) to 2500 V (i) deflection voltage.

4.3 Electron Energy Spectra

The entire detection unit was used to measure energy spectra, and tests without and with the laser were done to ensure the deflection unit performs in live measurements. The measurements in Figure 4.5 were done under the same conditions¹ on the left without the laser and on the right with laser pulsing switched on. In this experiment the sample Dielectric sample (seen in Figure 4.2) was used, which is transparent to the laser light, so the fact that these two measurements are very similar confirms that the laser does not contribute to the measurement and the deflection unit works.

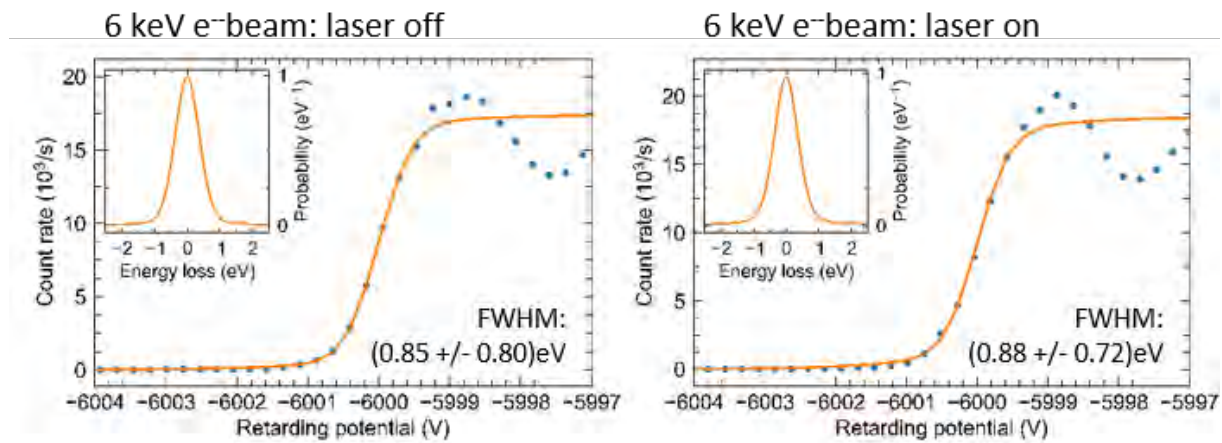


Figure 4.5: Measurements at 6 keV without and with the laser look identical.

We observe modulations in the number of counts for values of the retarding potential above the energy of the incoming electrons (-5999 to -5997 V in Figure 4.5). This can be attributed to the fact that the electron beam does not hit the same pixels on the detector throughout the measurement. Changing the retarding voltage changes the focus of the electron beam, and when the retarding potential approaches the energy of the incoming electrons, the initially focussed electron spot elongates into a stripe before the coulomb barrier is closed and fewer and fewer electrons arrive at the sensor. This increase in counts is correlated with the number of hit pixels on the detector, and as it seems that pixels have a decreasing sensitivity, the number of counts appears to increase.

These measurement was done with coarse temporal alignment of the laser and electron pulse on the scale of several nanoseconds. Temporal alignment is achieved by measuring the temporal position of the electron and laser pulse with respect to the trigger signal on the oscilloscope, and then varying the delay of the laser pulse. As the exact delay cannot be determined with absolute certainty in our setup, and temporal overlap is required to see PINEM, several measurements with different delay times within a 5.5 ns time-window were taken and analyzed. As we see in Figure 4.6, the measurements were very reproducible, but none of the measurement show an indication of the PINEM effect as calculated in Figure 2.3.

These measurements were taken with the "unit cell" approach, where the beam was not

¹Aperture 1, Spot 3.9, Blanker 1, Bullet 70 μm , 6 keV, Coulomb HV CT = 8000 V, C2 = 0.065

Blanking signal (Ch1): pulsed, 12.5 kHz, 5 Vpp, Pulse width 40 μs , Edge times 20 ns Laser trigger signal (Ch2): pulsed, 25.0 kHz, 1 Vpp, Pulse width 100 ns, Edge times 2.9 ns

Iseg SHR 2-Channel HV Supply HV offset: 5988.0 V Scanning range: 15.0 V Integration time T = 0.2 s (20 readings)

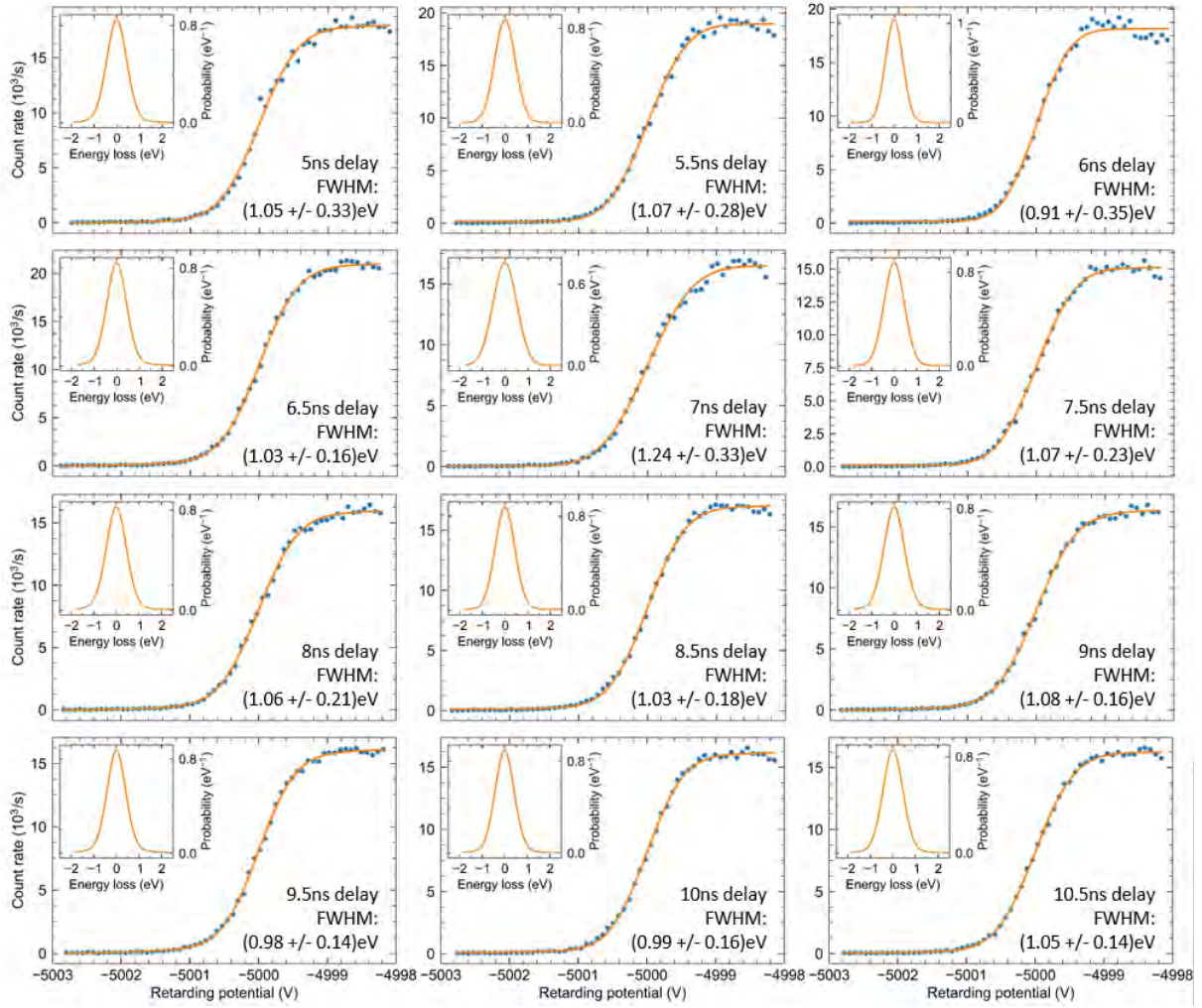


Figure 4.6: Hole array of 400 nm 200 nm 2x75 nm Au, tilted 20 degrees delay sweep laser on

focussed on a position going through a hole, but a single unit cell (equivalent to the unit cell in the simulation) to mitigate the effect of drift. This will decrease the expected β as we average across the entire hole, where there is little coupling in comparison to the regions close to the edge of the hole. We also use a tilted sample holder, as tilting the structure should produce higher beta values overall, as shown by [Wang et al. \(2020\)](#).

Results in [Figure 4.6](#) were measured on a holey Silicon Nitride membrane, covered with 75 nm Gold on both sides. It can be seen in [Figure 4.7b](#) and was simulated in [Figure 2.3](#). In the experiment, we were limited by the sample damage threshold (described in [section 4.4](#)).

4.4 Sample Damage

We observe that our samples sustain damage when exposed to high laser powers. Silicon Nitride membranes crack, Plasmonic samples covered with a thin metal layer melt locally (Figure 4.7). These damaged spots can be used to estimate the spot size of the laser beam, after it is coupled in through the half-parabolic mirror. From these images, we can estimate it to be around $5\text{ }\mu\text{m}$.

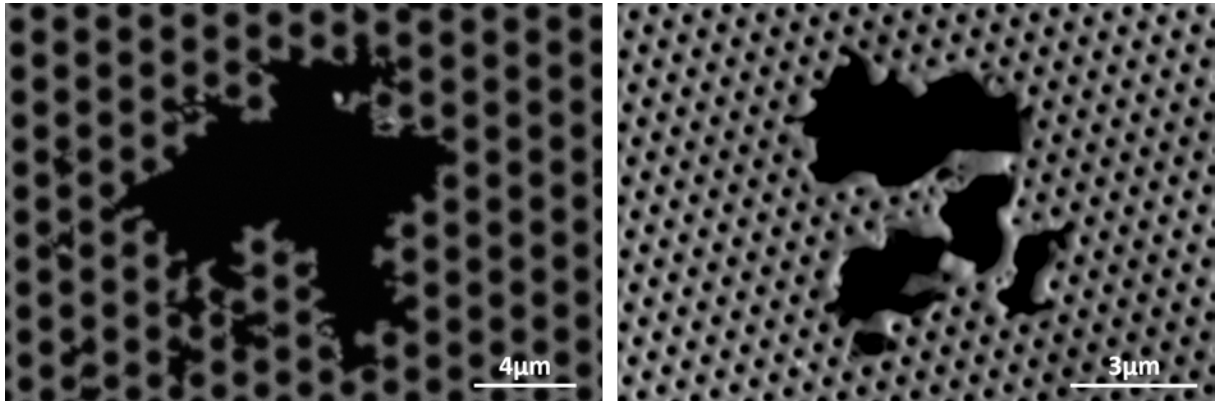


Figure 4.7: Membranes of Silicon Nitride only (left) and coated with Gold (right) damaged by laser irradiation.

We estimate that one third of the total laser power reaches the sample, due to losses in the light collection optics after the fibre coupling unit due to a rather large numerical aperture of the employed optical fibre. We start to observe gradual cracking of a silicon nitride membrane in Figure 4.8 at 37 mW and $1.48\text{ }\mu\text{J}$ Laser power, of which about one third reaches the sample. Using such high laser intensities is only enabled by the deflection unit protecting the detector. The Plasmonic sample started melting at powers of around 6 mW (of which we expect around 2 mW to reach the sample), which was taken as a basis for the recalculation of the expected β factors in Figure 2.3.

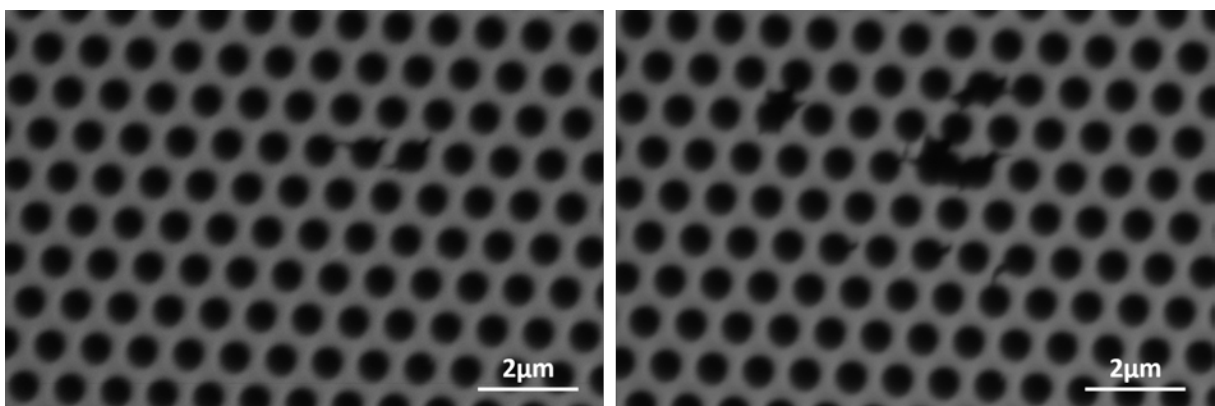


Figure 4.8: Exposing the silicon nitride membrane to 32 mW and 38 mW laser power leads to cracking of the structure.

These new findings of the damage threshold of our nanostructures allowed to re-calculate the coupling factor and PINEM spectra that we were able to use before any damage was visible. The updated simulation results (shown in Figure 2.3) indicate that even under perfect

conditions (no drift, electron beam in the optimal position), it would have been challenging to measure PINEM. In our differential measurement, PINEM side-bands appear as small deviations in the slope of the measured energy scan, which makes it hard to resolve them in the presence of statistical fluctuations and experimental instabilities even though the energy resolution of the detector is high enough.

Given these limitations of the laser intensity that can be used on Silicon Nitride membrane samples, a tungsten needle, which has a much higher melting point and is expected to have a higher damage threshold, was used as a probe [Figure 4.9](#). [Shiloh et al. \(2021\)](#) showed PINEM with a similar Tungsten needle at low electron energies. Even the tip of the needle was severely damaged when exposed to the laser.

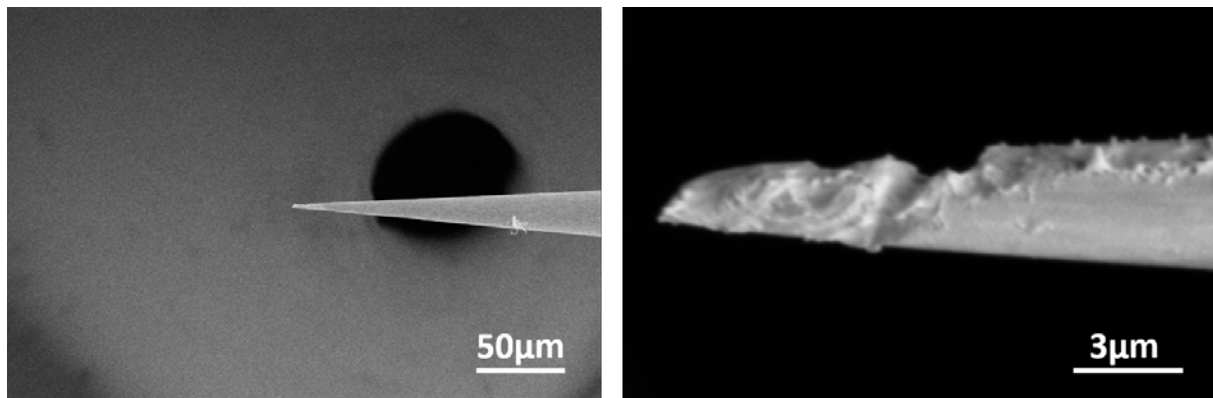


Figure 4.9: Tungsten needle after laser exposure of 1.8 mW is also heavily damaged

We find that the deflection unit effectively shields the detector from laser light and bends the electron path, the RFA measurements show agreement with simulations and we record very reliable and reproducible measurements. Unfortunately, our samples were damaged by the laser power we are using.

Chapter 5

Conclusion and outlook

We designed a highly sensitive system to measure PINEM side-bands in the electron energy spectrum in a Scanning Electron Microscope. Simulations of the Retarding Field Analyzer show an intrinsic energy resolution of 0.09 ± 0.02 eV for 4 kV, 0.11 ± 0.03 eV for 5 kV and 0.13 ± 0.04 eV for 6 kV electrons. This is much smaller than the thermal spread of our electron source (around 0.8 eV) and enables us to resolve the spacing of the side-bands in our setup (1.2 eV) at these low electron energies.

Measurements at extremely small currents were taken, which was made possible by introducing a single-electron detector with a cooling unit into the system. As this highly sensitive, pixellated detector also detects signal from the laser, a deflection unit that blocks the light and guides the electrons through was designed and tested. With these elements, measurements under experimental conditions for PINEM are now very reliable and reproducible.

Further, nanostructures were simulated (FDTD) and PINEM coupling parameters were calculated in order to choose a structure with which a strong PINEM effect can be seen. Experiments showed, that we did not reach sufficiently high fields before the structures started to be damaged, so the PINEM effect could not be measured yet. However, all the infrastructure is in place to run further experiments.

Outlook

The main limitation of the current setup is the damage that the samples sustain from being exposed to the laser irradiation. There are several possible solutions to avoid this problem. Our nanostructures are not optimised to be resonant at the wavelength of our laser. Resonant nanostructures would produce higher local field intensities with lower input power. These nanostructures could either be optimized hole arrays, similar to the ones we are currently using, with different metal coatings, or small resonant structures like nanorods, dropcast onto the membrane. Apart from being resonant to the laser, these structures must also ensure that the electron beam can pass the near-field without getting stuck in the carrier membrane.

An option that we have started to explore is the use of tougher materials, for example a tungsten needle, which has been used by [Shiloh et al. \(2021\)](#), first also observed on carbon nanotubes ([Barwick et al., 2009](#)). For these, the alignment of the tip with respect to the accepted radius of the RFA is challenging and currently done with adhesive tape by eye.

Another pathway is to use shorter laser pulses, an option that is available in a pump-probe setup, which is also available in the group ([Solà Garcia, 2021](#)). In this setup, the electron pulses are excited by a higher harmonic of the laser that is coupled into the chamber, which enables much shorter (femtosecond) laser pulses that are less damaging. Furthermore, we can benefit from using a shorter wavelength laser, 517 nm which corresponds to 2.4 eV and side-bands that are spaced further apart. However, in that setup, spatial resolution is limited, and measurements would have to be taken with a periodic structure, such as a nanohole array, as it is not possible to focus on small structures. In order to do this, the entire RFA and deflection unit was further reduced in height, as the space in the chamber is limited. After we made some modifications, the device is ready to be tested in that setup.

This thesis is a proof of concept of a novel way to measure PINEM in an SEM, and provides the technical capabilities. There is a lot of room for improvement by carefully designing the nanostructure. While we assume that the optical pulse is longer than the electron pulse, which means that the electron can be viewed as a classical particle, our setup can serve as flexible platform for future experiments that explore the quantum nature of non-relativistic electron wave packets and how its wave function can be shaped with optical near-fields ([Carbone, 2021](#)).

Appendix A

Setting up an experiment

Check setup before starting

CL system

Start the CL computer (in the rack) by pressing the small button on the PC.

User: sparc, password: delmic Plug in the cooling of the delmic Spectrometer at the back of the system into the wall - this needs to be unplugged after use

Set switch to position 1

Connect the ground of the SEM to the copper bar on the wall

Start Odemis

Check that \ (SPARC2_FIBER_VISNIR) is starting up, all the modules should be indicated

Wait for everything to initialize

Ensure the piece of plastic is not in the spectrometer in the delmic box

Laser

Switch on laser software

Alignment

Switch on Keithley on the right and check ZCHK

Diode: Start power supply for Diode before switching it on

SEM

Write down the vacuum values into the log sheet

Vent chamber

Put in sample and take a Nav-cam picture before closing the chamber

Bullet 70um in for PINEM, check whether it's there and mounted properly. It needs to be fully inserted, otherwise the CL mirror might hit it.

Close chamber (check all cables inside are fine), hold the door closed and pump)

When the vacuum is below 10^{*-5} , ideally 10^{*-6} , turn on the beam

Check that beam shift is zeroed

Blanker 1

Aperture 1

Focus on the sample:

5th tab - gun alignment

Mirror alignment

Check chamber to ensure the stage is in a position where the mirror fits

Go to odemis, click park mirror to reference it

Click engage mirror

In the SEM, zoom out and check that the hole of the mirror is in the centre of the image

If it is not the case, go to the alignment tab in odemis (upper right) and move the hole to the middle of the screen

Switch off chamber illumination by pausing the chamber video

Blank ebeam

Focus on the aperture on the diode (or a material with lots of CL intensity)

Set beam to external before changing to odemis

Go to odemis

Go to the alignment tab

Click lens (should be green)

Click autofocus

Set exposure time to 2s for rough alignment, later go to shorter times and less outliers

Blue stuff is moving

Move up sample in z direction until it is a parabola shape

Then adjust x and y to make it into the smallest possible point

Change to the SEM (full scan) to re-focus and change back to external to odemis to do it again

Exp time 500ms

Binning 2

Gain 16-bit

Readout 100MHz

For a 5keV, Spot 3.9 Ct=6000V C2=0.15 the counts were around 20000 at z=13.957mm

Check again in the SEM to ensure beam shift is set to 0

Fibre alignment

Blank the beam, connect Keithly (yellow cable) to the correct diode

Turn on Keithley

Press I for current

Press up arrow for maximum range

Press auto

Switch on the pointing diode on the right of the laser with the small switch

Unblank beam

On Keithley, press ZCHK button. With diode on it was around 1.6uA

Go to Odemis fiber aligner

On the odemis fiber aligner, move in x and y direction to maximise the signal. This was around 2uA

Read out fiber alignment

Go to terminal

(cd usr/share/odemis)

(Odemis-cli --list-prop \fiber-aligner")

Read out position (RO vigilant attribute)

$x=0.0103644966$

$y=-0.09836448328$

Move stage manually to check whether you are at the maximum

Switch off pointing diode

Keithley: press ZCHK

Laser Move to the other diode manually - go to the border next to the diode to make sure you do not overload the amplifier when switching on the laser

Install magnetic shield in the delmic unit

Turn laser key to position 1 (wait 20 min for stable laser signal)

Oscilloscope: set to 10V 1M Ω to make sure nothing breaks

Laser: interlock, all screws are on properly

Set laser to external trigger in "AOT" and stepper to 0(%)

Set laser key to position 2

Press start pulsing on the laser software

SEM

Acceleration voltage	C_2 setting	C_t setting
30keV	$C_2=0.432$	
20keV	$C_2=0.366$	$C_t=3333V$
10keV	$C_2=0.258$	
7.5keV	$C_2=0.258$	
6keV	$C_2=0.065$	
5keV	$C_2=0.15$	$C_t=6000V$

Table A.1: C_2 values for different currents at spot 3.9

Appendix B

Data sets

V start [V]	V step [V]	init loc [mm]	init angle [deg]	acc V	energy distr	marks	electrons	runs	notes
3998	0.01	10, 36.9, 10	0.143	4	sharp	2	100	400	
3998	0.01	10, 36.9, 10	0.143	4	gauss FWHM 0.8 eV	2	100	400	
4998	0.01	10, 36.9, 10	0.143	5	sharp	2	100	400	
4998	0.01	10, 36.9, 10	0.143	5	gauss FWHM 0.8 eV	2	100	400	
5998	0.01	10, 36.9, 10	0.143	6	sharp	2	100	400	
5998	0.01	10, 36.9, 10	0.143	6	gauss FWHM 0.8 eV	2	100	400	
5998	0.01	10.01, 36.9, 10	0.143	6	sharp	2	100	400	x offset
5998	0.01	10.02, 36.9, 10	0.143	6	sharp	2	100	400	x offset
5998	0.01	10.03, 36.9, 10	0.143	6	sharp	2	100	400	x offset
5998	0.01	10.04, 36.9, 10	0.143	6	sharp	2	100	400	x offset

Table B.1: Simulation data sets of the entire RFA and deflection unit with the sample (SIMION)

Appendix C

MiniPix Detection

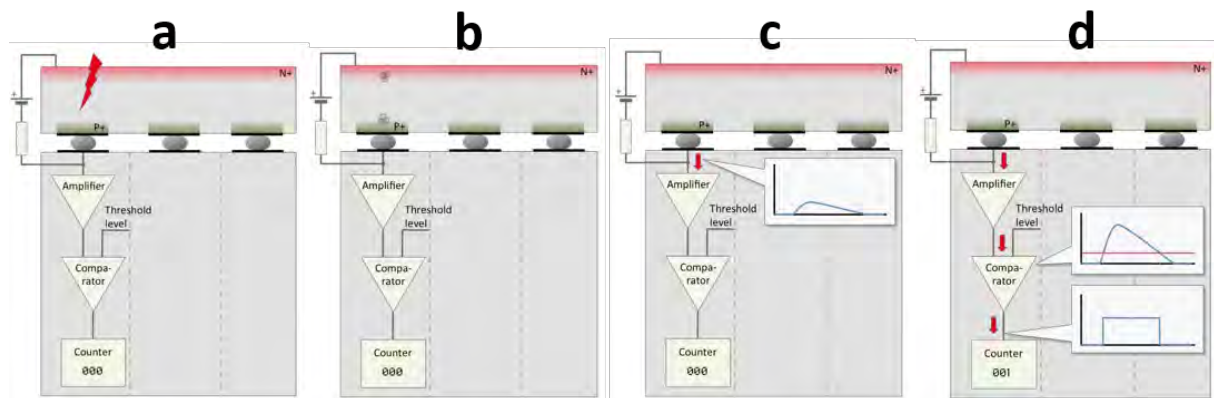


Figure C.1: (a) A photon/electron impinges on the 200nm thick Si layer and (b) creates electron-hole pairs, which move towards the electrodes due to an applied field. (c) The signal is amplified, (d) compared to the set threshold and counted if it is above. The amount of time the signal is above the threshold is also recorded.

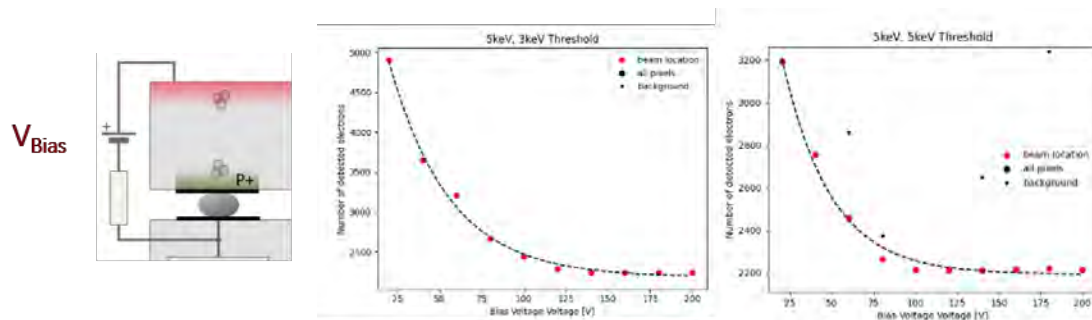


Figure C.2: Measurements for different bias voltages

Appendix D

Code

D.1 Electron Trajectories

D.2 SIMION script

This script can be used to simulate voltage sweeps on imported files. Ensure that the correct electrodes is selected.

```
simion.workbench_program()

-- variables
adjustable voltage = -5999          -- starting voltage
adjustable del_voltage = 0.01       -- voltage steps
adjustable n_runs = 300             -- number of runs

-- uncommenting this function enables to count particles
-- at a specified y position
--function segment.other_actions()
--  if ion_py_mm <= 16.89 then
--    mark()
--    ion_splat = 1
--  end
--end

-- This runs the programme while changing the scanning voltage
function segment.terminate()
if ion_number == 1 then
    voltage = voltage - del_voltage
    n_runs = n_runs -1
    sim_rerun_flym = (n_runs > 0) and 1 or 0
end
end

end
```

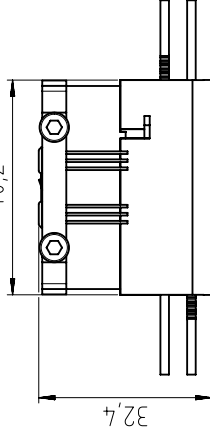
```
function segment.fast_adjust()  
adj_elect03 = voltage  
  
end
```

Appendix E

Technical Drawings

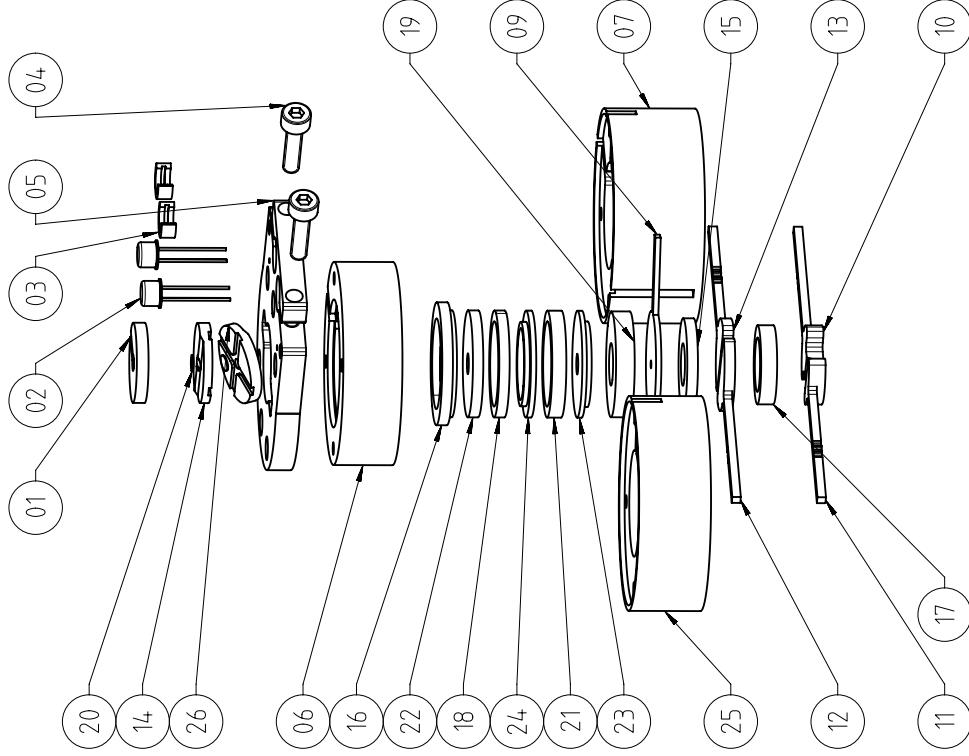
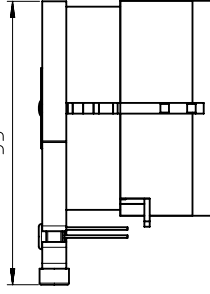
Technical drawings of the important components for the deflection unit, scaled down to A4.
All drawings were done by Max Postma M.Postma@amolf.nl

40,2



32,4

53



26	1	Slanted sample holder	15	AL6082	-
25	1	Minipix adapter		PEEK	-
24	1	Lens 3		VAR	-
23	1	Lens 4		VAR	-
22	1	Lens 2		VAR	-
21	1	RFA spacer 2		VAR	-
20	2	Sample		VAR	-
19	1	Repel spacer 3		MACOR	-
18	1	RFA spacer 1		VAR	-
17	1	Repel spacer 2		MACOR	-
16	1	RFA spacer 3		VAR	-
15	1	Repel spacer 1		MACOR	-
14	1	Slanted sample holder	20	AL6082	-
13	1	Grounding repel plate 1		Ti	-
12	1	High voltage repel plate 1		Ti	-
11	1	Grounding repel plate 2		Ti	-
10	1	High voltage repel plate 2		Ti	-
09	1	Lens 1		VAR	-
07	1	Electron repelling adapter		PEEK	-
06	1	RFA Macor NX		MACOR	-
05	1	RFA lid		Ti	-
04	2	Inbus M3X12		RVS304	-
03	2	Diode insulator		PEEK	-
02	2	Diode		VAR	-
01	1	Sample holder		AL6082	-
Item	Qty	Partname		Material	

Partnumber/Remarks				
	Date	Name		
DRN	30-09-2021	AMH		
PRD	21-03-2022	AMH		
General tolerances unless otherwise specified ISO-2768-MH-E	Geometrical tolerances unless otherwise specified ISO-8015-E	Surface roughness of milled surfaces unless otherwise specified 3,2 Ra (maximum standard) 1,6 Ra (finishing typical)		
Size	Partnumber:			
A3	NANOC-15-11-00			
Number of sheets: 1 of 1				

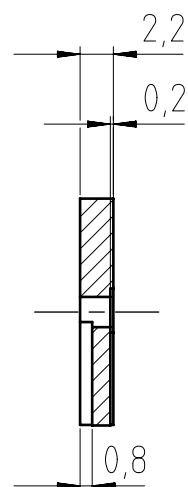
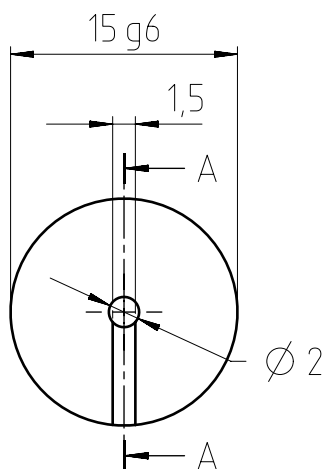
NanoCenter

15 Verios-Simplified RFA setup

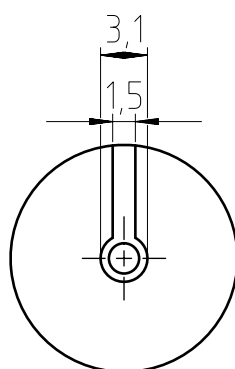
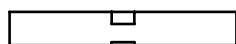
Scale: 1:1	0	50	Dim in mm
------------	---	----	-----------


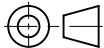




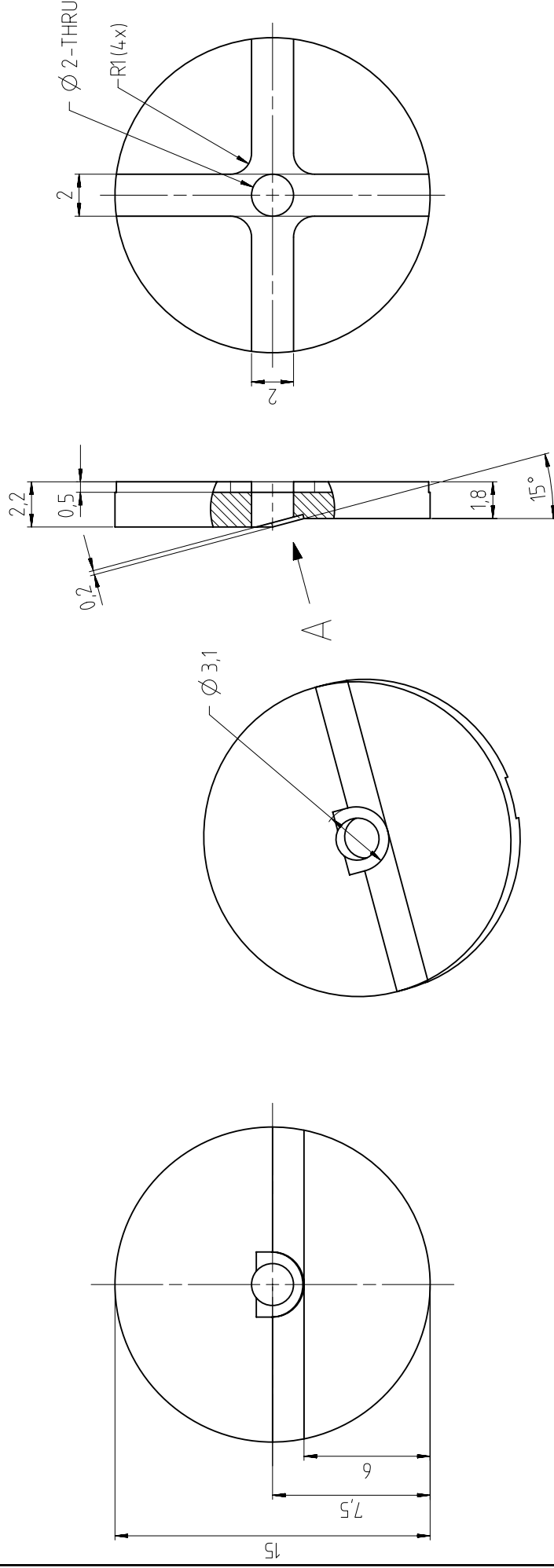
NANOC-15-11-00




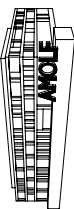

Doorsnede A-A

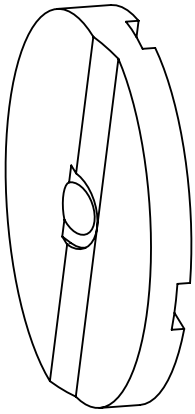
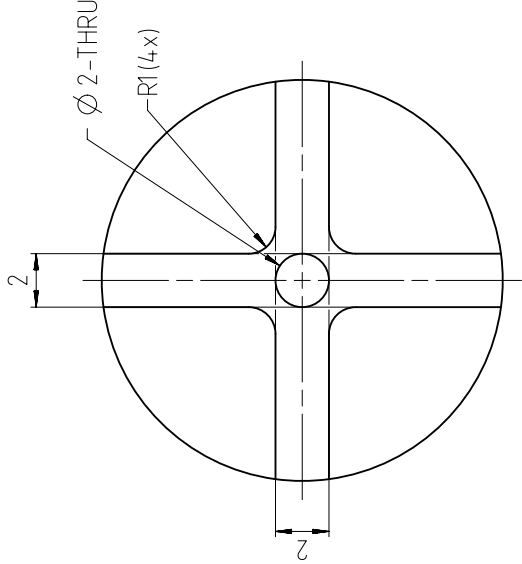
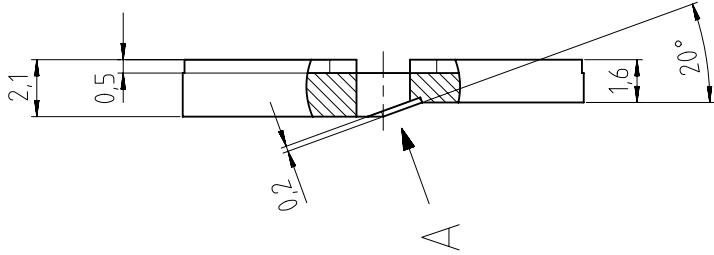
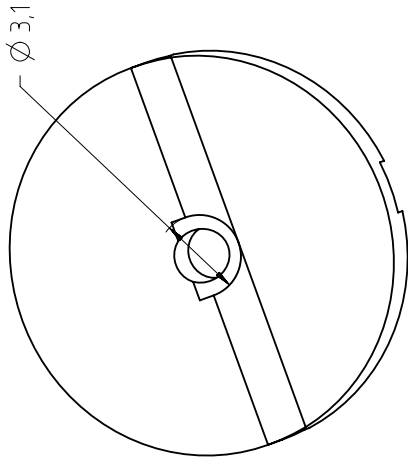
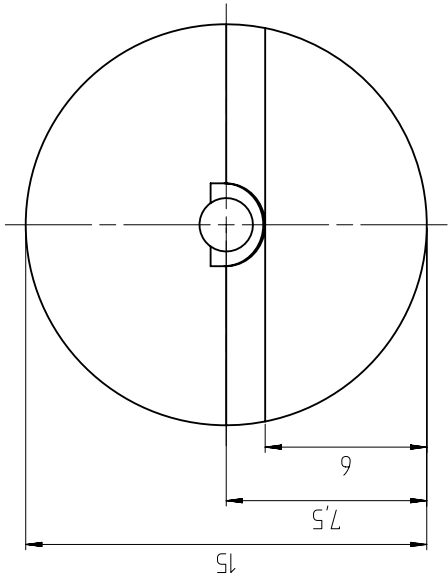


01	5	Sample holder	AL6082			
Item	Qty	Partname	Material	Partnumber/Remarks		
<h1>NanoCenter</h1> <p>15 Verios-Simplified RFA setup</p>					Date	Name
				DRN	05-08-2021	AMH
				PRD	18-03-2022	AMH
scale: 2:1			 Dim.in mm	General tolerances unless otherwise specified ISO-2768-fH-E	Geometrical tolerances unless otherwise specified ISO-8015-E	Surface roughness of machined surfaces unless otherwise specified 3,2 Ra (maximum standard 1,6 Ra (fitting typical))
 				Size A₄	Partnumber: NANOC-15-11-01	
				Number of sheets: 1 of 1		


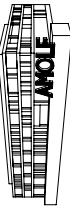



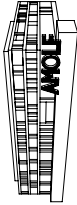
VIEW A

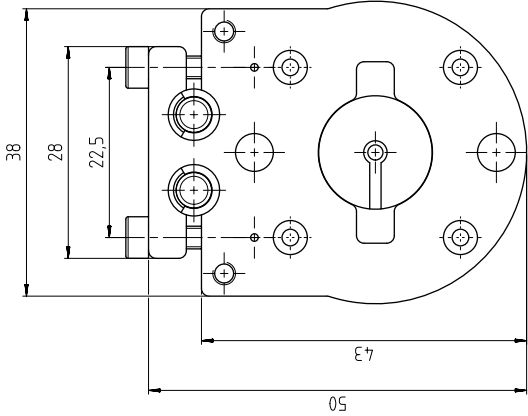
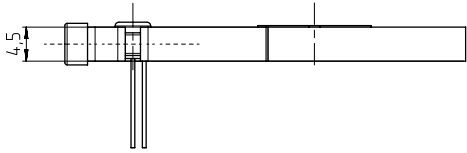
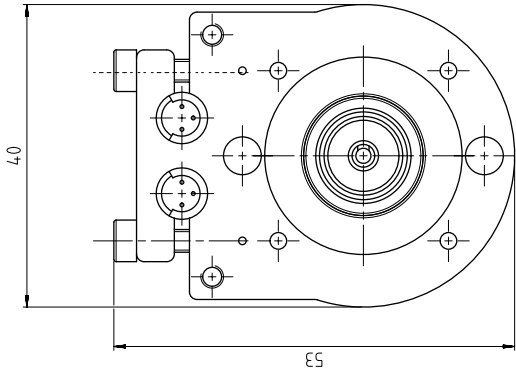
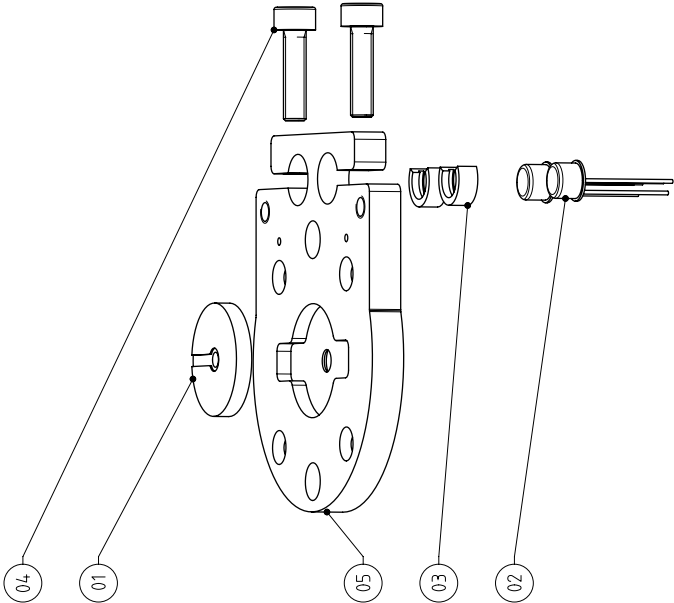
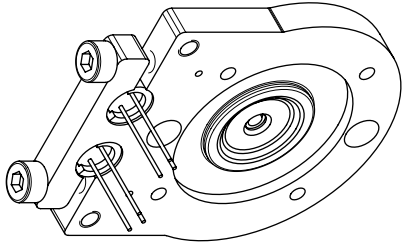
26	1	Slanted sample holder 15	AL6082
Item	Qty	Partname	Material
<div> <div> <h1>NanoCenter</h1> <h2>15 Verios-Simplified RFA setup</h2> </div> <div>   </div> </div>			
scale: 5:1		<div> <div>0</div> <div>10</div> </div>	<div>  <div>Dim in mm</div> </div>
General tolerances unless otherwise specified ISO-2768-MH-E		Geometrical tolerances unless otherwise specified ISO-8015-E	Surface roughness of milled surfaces unless otherwise specified 3.2 Ra (maximum standard) 1.6 Ra (finishing spec)
Date		Name	
DRN 05-08-2021		AMH	
PRD 18-03-2022		AMH	
Partnumber/Remarks			
Size		Partnumber	
A3		NANOC-15-11-26	
		Number of sheets: 1 of 1	



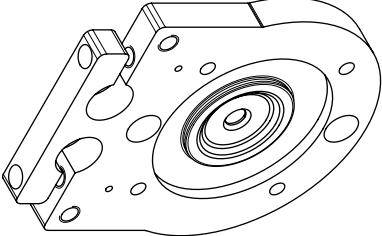
VIEW A

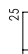




































































14	1	Slanted sample holder 20	AL6082						
Item	Qty	Partname	Material	Partnumber/Remarks					
NanoCenter							Date		Name
15 Verios-Simplified RFA setup							DRN	05-08-2021	AMH
							PRD	18-03-2022	AMH
				General Tolerances unless otherwise specified ISO-2768-MH-E	Geometrical Tolerances unless otherwise specified ISO-8015-E	Surface roughness of milled surfaces unless otherwise specified 3,2 Ra (maximum standard) 1,6 Ra (finishing typical)			
scale: 5:1		0		10				Dim in mm	
									
A.M.O.E.F						Size			
						Partnumber:		NANOC-15-11-14	
						A3		Number of sheets: 1 of 1	

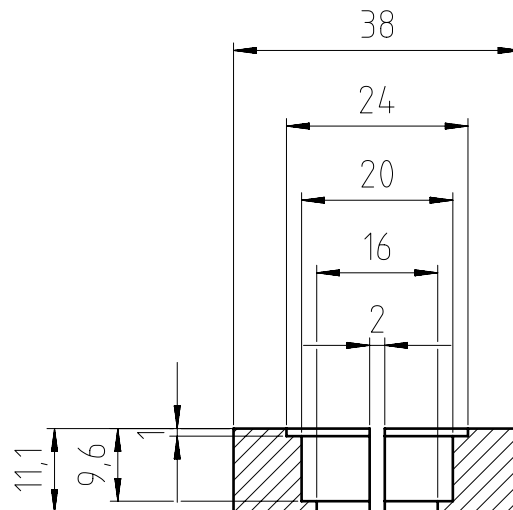
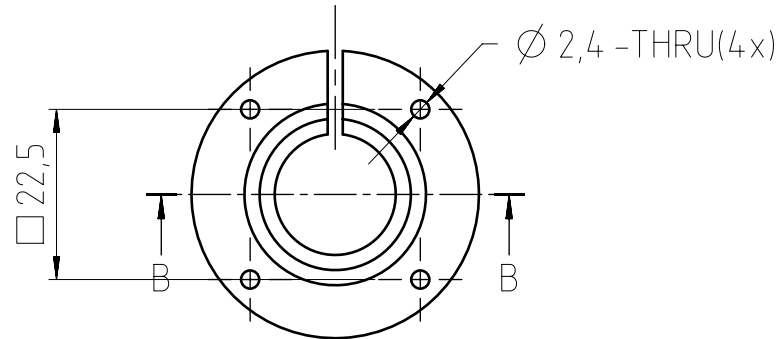
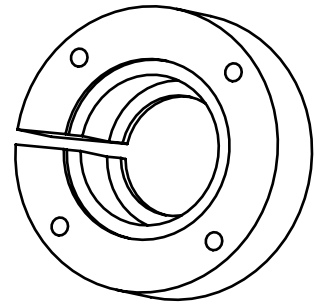




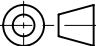


05	1	RFI lid	Ti	-
04	2	Inbus M3X12	RVS304	-
03	2	Diode insulator	PEEK	-
02	2	Diode	VAR	-
01	1	Sample holder	AL6082	-
Item		Qty	Partname	Material
NanoCenter				
1.5 Verios-Simplified RFA setup				
Partnumber/Remarks				
DRN		Date		Name
PRD		18-03-2022		AMH
General tolerances		Geometrical tolerances		Surface roughness
ISO-2768-TH-E		otherwise specified		unless otherwise specified
ISO-8015-E		ISO-8015-E		ISO 10000 standard
ISO 10000 standard		ISO 10000 standard		ISO 10000 standard
Size		Partnumber		Partnumber
A2		NANOC-15-11-08		NANOC-15-11-08
Number of sheets		1 of 1		1 of 1



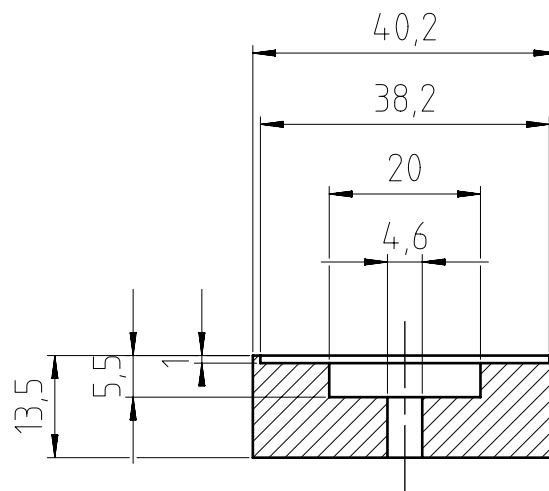
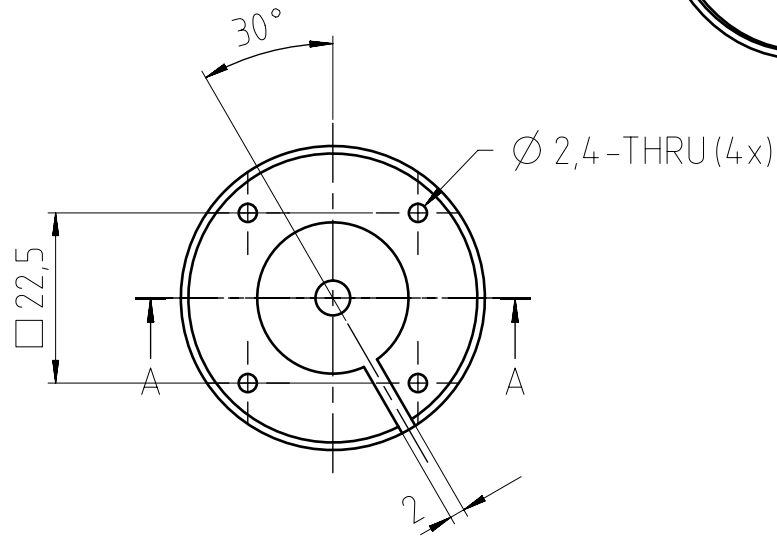
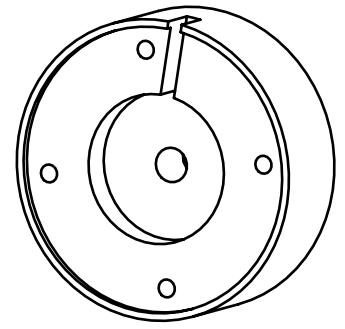
05	1	RFA	lid		Ti
Item	Qty	Partname	Material		
NanoCenter					
15 Verios-Simplified RFA setup					
scale: 2:1		0		25	Dim in mm
					
					
					
					
					
					
					
					
					
					
					
					
					
					
					
					
					
					
					
					
					
					
					
					
					
					
					
					
					
					
					
					
					
					
					
					
					
					
					
					
					
					
					
					
					
					
					
					
					
					
					
					
					
					
					
					
					
					
					
					
					
					
					
					
					
					
					
					



Doorsnede B-B

06	1	RFA Macor NX	MACOR				
Item	Qty	Partname	Material	Partnumber/Remarks			
<div>NanoCenter</div> <div>15 Verios-Simplified RFA setup</div>					Date	Name	
				DRN	30-09-2021	AMH	
				PRD	18-03-2022	AMH	
scale: 1:1		<div>050</div> <div></div>	<div></div> <div>Dim in mm</div>	General tolerances unless otherwise specified ISO-2768-fH-E		Geometrical tolerances unless otherwise specified ISO-8015-E	Surface roughness of machined surfaces unless otherwise specified 3,2 Ra (maximum standard) 1,6 Ra (fitting typical)
<div></div> <div></div>				Size	Partnumber:		
				A4	NANOC-15-11-06		
				Number of sheets: 1 of 1			

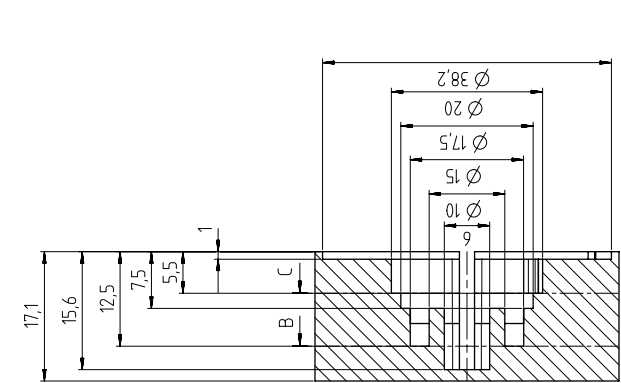
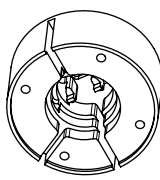
This drawing may not be used for commercial purposes without written authorisation



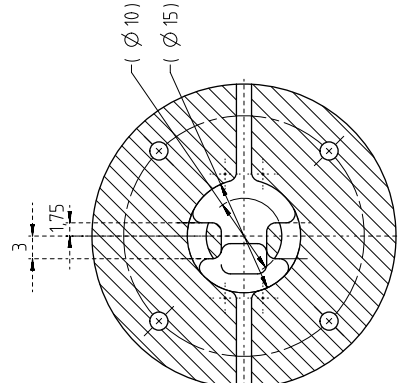
Doorsnede A-A

This drawing may not be used for commercial purposes without written authorisation

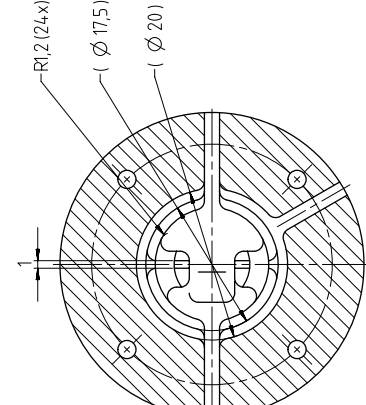
25	1	Minipix adapter	PEEK				
Item	Qty	Partname	Material	Partnumber/Remarks			
<div>NanoCenter</div> <div>15 Verios-Simplified RFA setup</div>					Date	Name	
				DRN	30-09-2021	AMH	
				PRD	18-03-2022	AMH	
scale: 1:1		<div>050</div> <div><div></div><div></div><div></div><div></div><div></div></div>		General tolerances unless otherwise specified ISO-2768-FH-E		Geometrical tolerances unless otherwise specified ISO-8015-E	Surface roughness of machined surfaces unless otherwise specified 3,2 Ra (maximum standard) 1,6 Ra (fitting typical)
<div><div>AMOLF</div><div><div></div><div>AMOLF</div></div></div>				Size A4	Partnumber: NANOC-15-11-25		
				Number of sheets: 1 of 1			



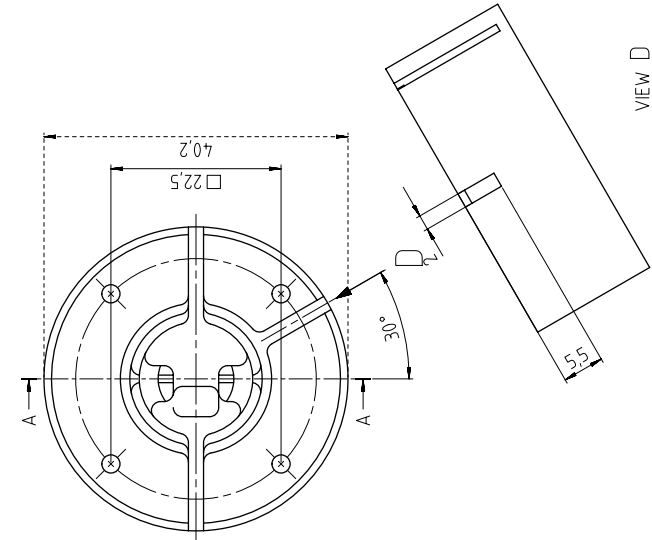
Doorsnede A-A



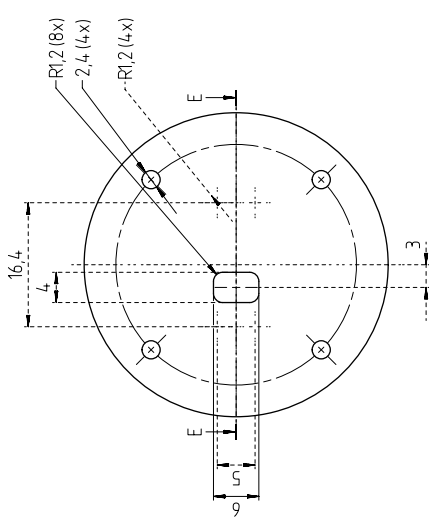
Doorsnede B-B



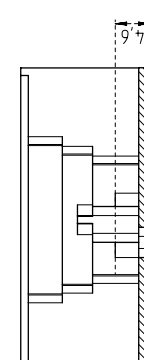
Doorsnede C-C



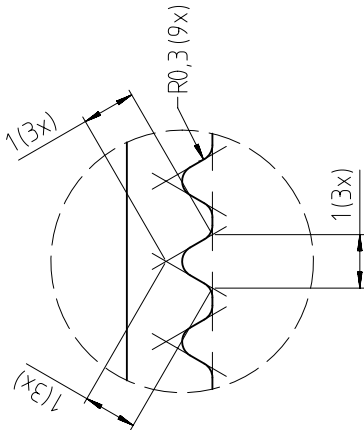
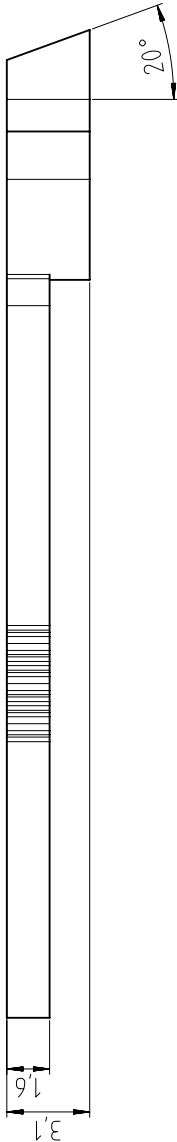
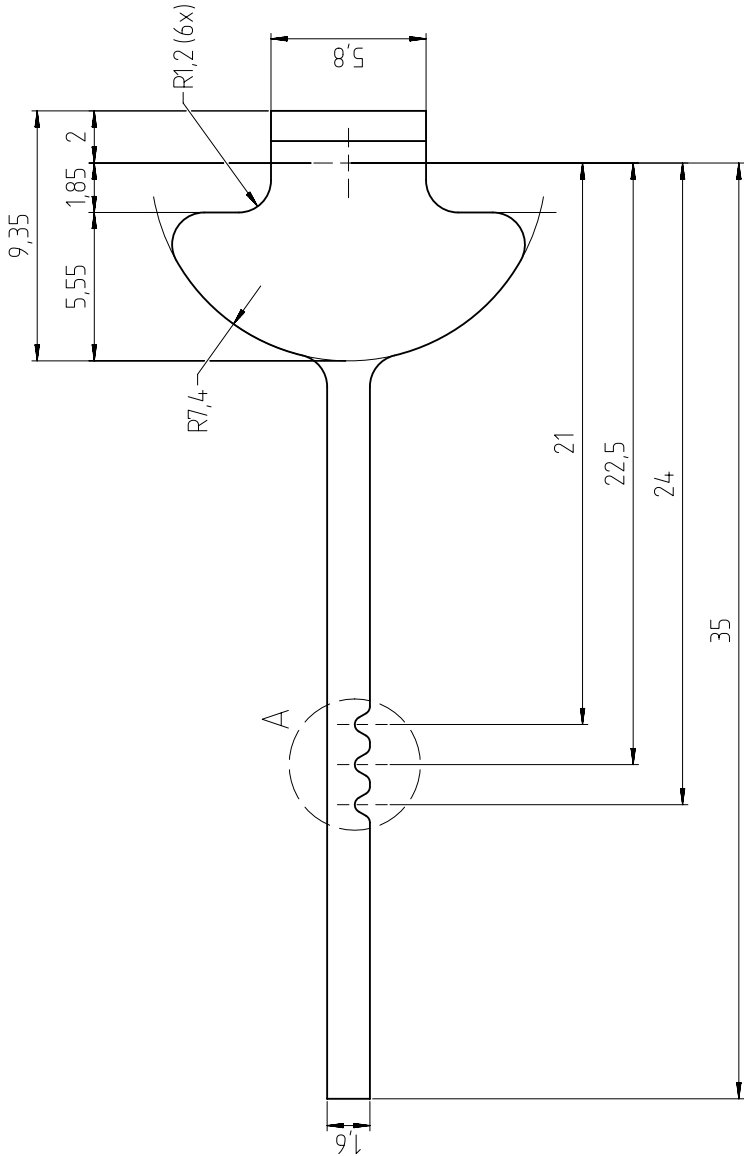
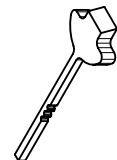
VIEW D



Doorsnede E-E

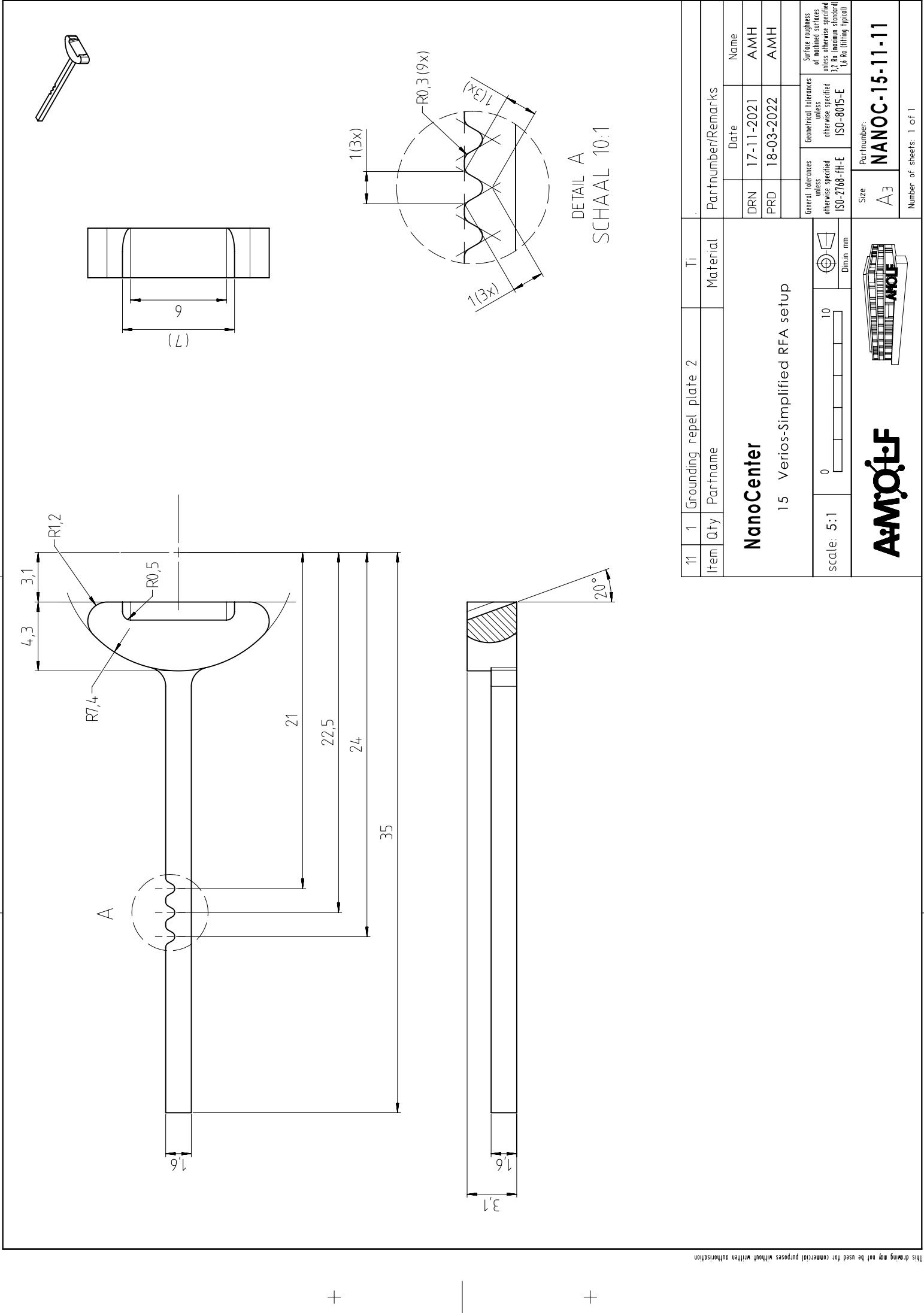


Item	Qty	Electron repelling adapter	Material	PEEK	Partnumber/Remarks
07	1	Electron repelling adapter	PEEK		
NanoCenter					
1.5 Verios-Simplified RFA setup					
scale: 2:1					
0 25 50 75 100 125 150 175 200 225 250 275 300 325 350 375 400 425 450 475 500 525 550 575 600 625 650 675 700 725 750 775 800 825 850 875 900 925 950 975 1000					
Din in mm					
General tolerances unless otherwise specified ISO 2768-TH-E					
Surface roughness unless otherwise specified Ra 0.8 (maximum standard) Ra 0.4 (finishing typical)					
Partnumber					
Size					
A2					
Partnumber					
NANOC-15-11-07					
Number of sheets 1 of 1					

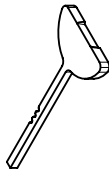
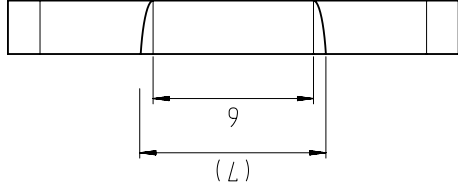
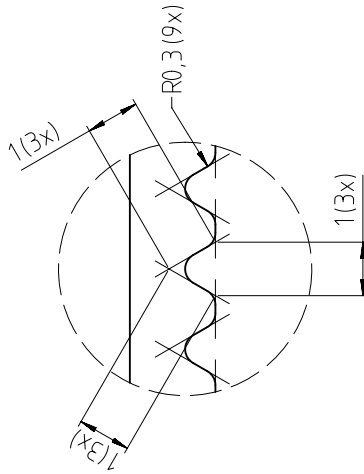
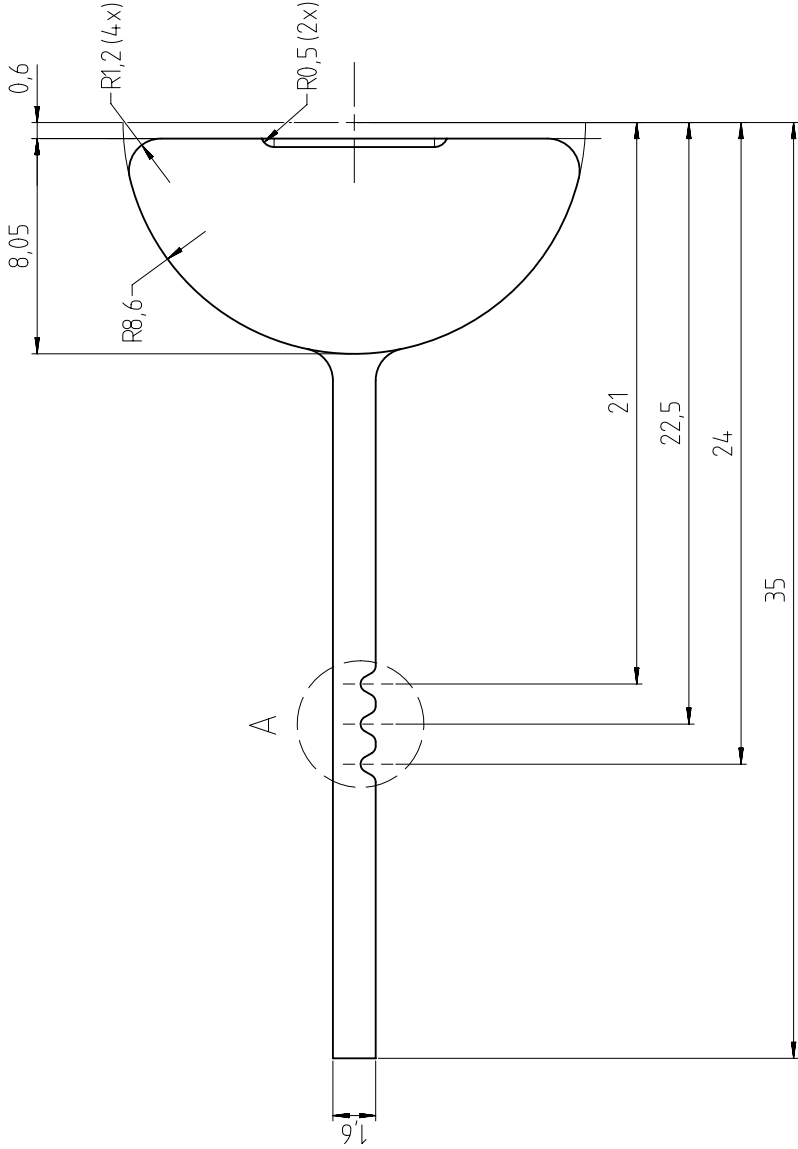


DETAIL A
SCHAAL 10:1

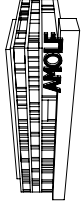
10	1	High voltage repel plate 2	Ti										
Item	Qty	Partname	Material	Partnumber/Remarks									
NanoCenter				15 Verios-Simplified RFA setup									
scale: 5:1		0		Dim in mm									
						General tolerances unless otherwise specified ISO-2768-MH-E			Geometrical tolerances unless otherwise specified ISO-8015-E	Surface roughness of milled surfaces unless otherwise specified 3,2 Ra (maximum standard) 1,6 Ra (finishing typical)			
A&M Q&F						Size		Partnumber:					
						A3		NANOC-15-11-10					
				Number of sheets: 1 of 1									

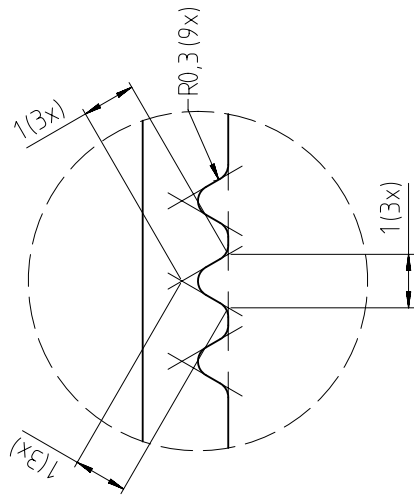
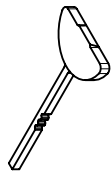
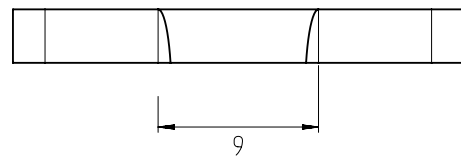
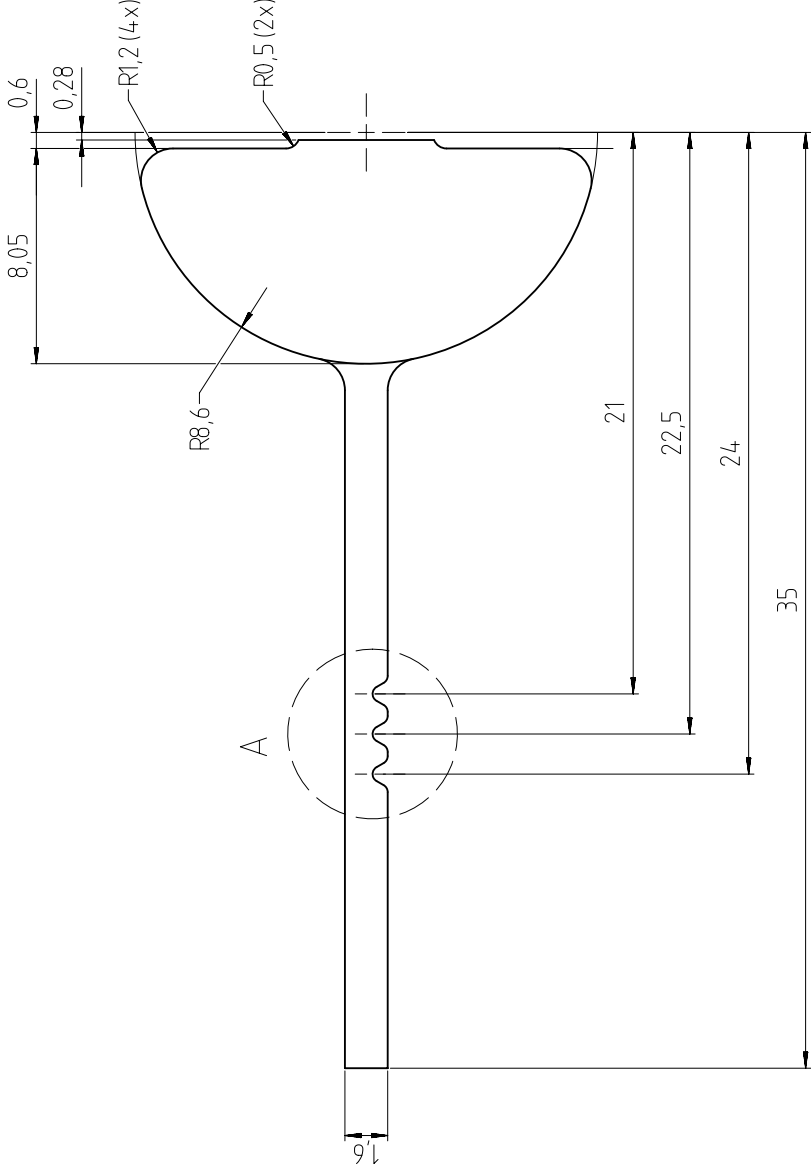


11	1	Grounding repel plate 2	Ti	
Item	Qty	Partname	Material	Partnumber/Remarks
NanoCenter				
15 Verios-Simplified RFA setup				
Scale: 5:1	0	10	Dim in mm	
				Surface roughness of milled surfaces unless otherwise specified 3,2 Ra (maximum standard) 1,6 Ra (finishing typical)
				General Tolerances unless otherwise specified ISO-2768-FH-E
				Geometrical Tolerances unless otherwise specified ISO-8015-E
				Date
				Name
				DRN 17-11-2021 AMH
				PRD 18-03-2022 AMH
				Size
				Partnumber: NANOC-15-11-11
				Number of sheets: 1 of 1



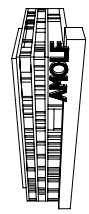
12	1	High voltage repel plate 1	Ti		
Item	Qty	Partname	Material	Partnumber/Remarks	
NanoCenter 15 Verios-Simplified RFA setup				DRN	17-11-2021 AMH
				PRD	18-03-2022 AMH
Scale: 5:1		0		Dim in mm	
				General tolerances unless otherwise specified ISO-2768-MT-E	Geometrical tolerances unless otherwise specified ISO-8015-E
				Surface roughness of milled surfaces unless otherwise specified 3.2 Ra (maximum standard) 1.6 Ra (tilling typical)	
			Size	Partnumber:	
			A3	NANOC-15-11-12	
			Number of sheets: 1 of 1		

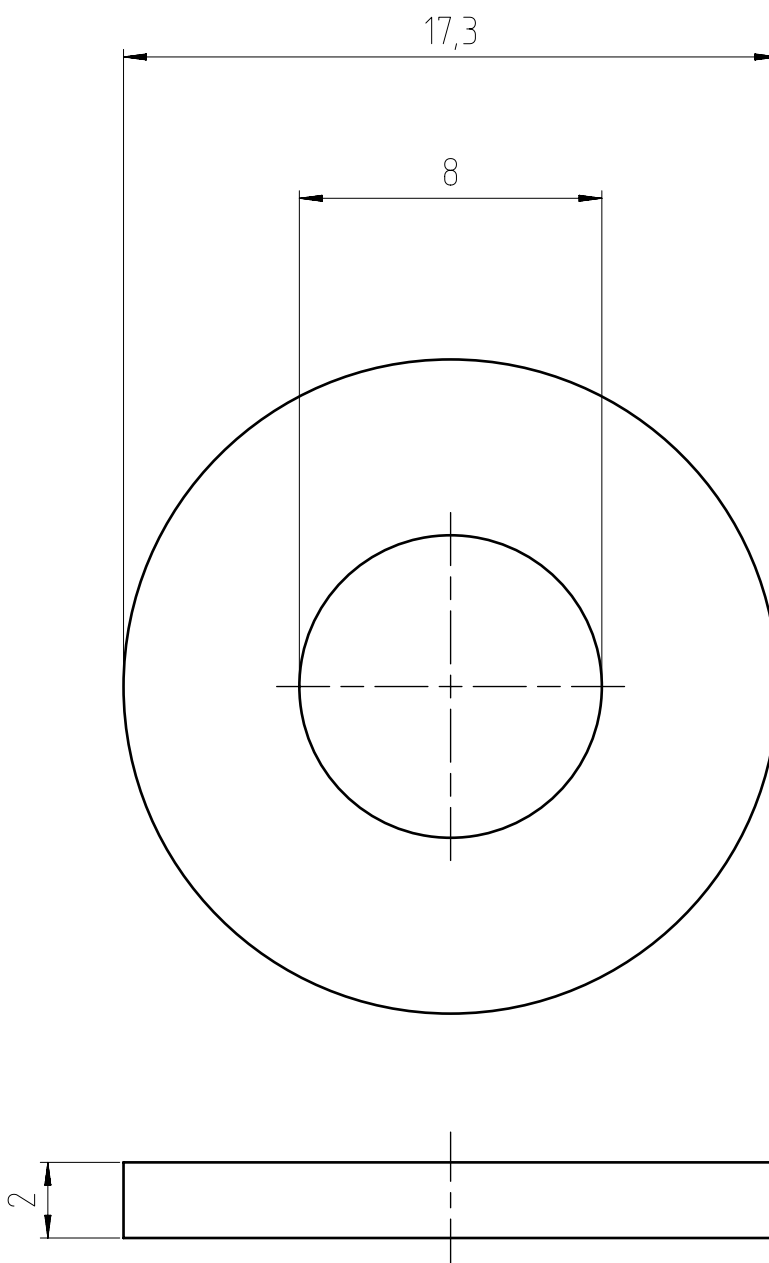
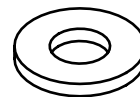




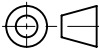


DETAIL A
SCHAAL 10:1

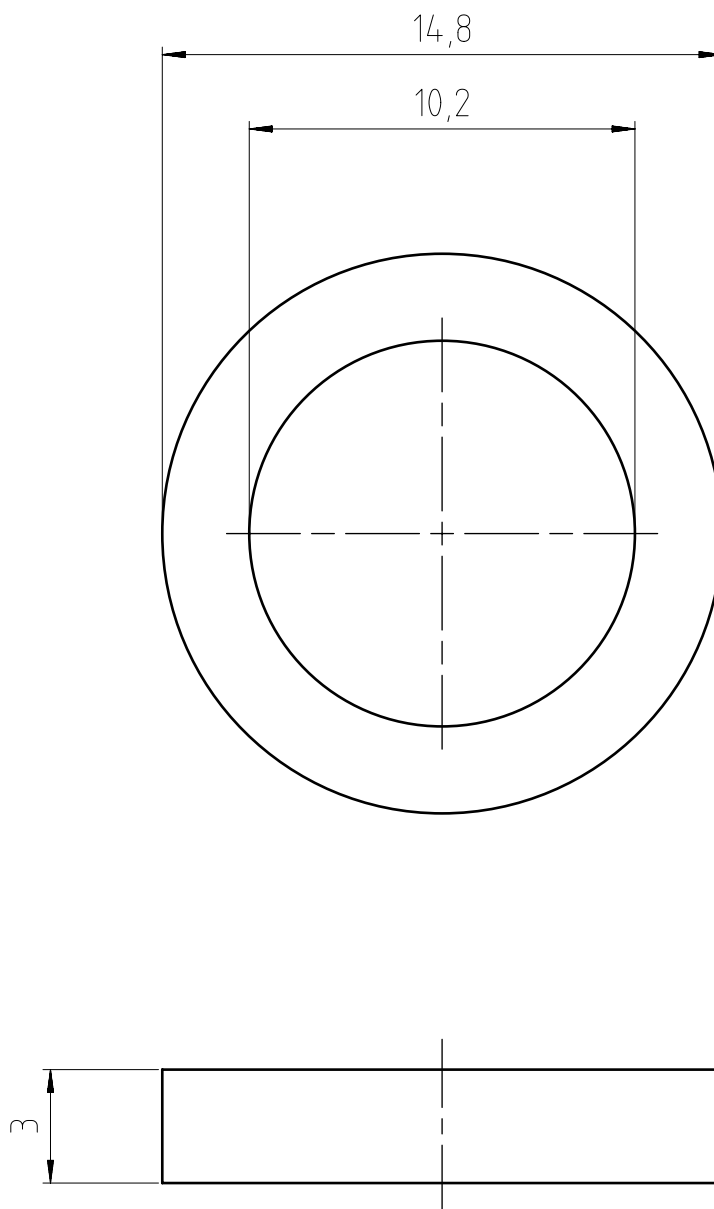
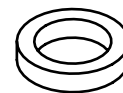
13	1	Grounding repel plate 1	Ti	
Item	Qty	Partname	Material	Partnumber/Remarks
NanoCenter				
15 Verios-Simplified RFA setup				
scale: 5:1	0	10	Dim in mm	
General tolerances unless otherwise specified ISO-2768-MT-E				
Geometrical tolerances unless otherwise specified ISO-8015-E				
Surface roughness of milled surfaces unless otherwise specified 3,2 Ra (maximum standard) 1,6 Ra (finishing typical)				
Date 17-11-2021 Name AMH				
Date 18-03-2022 Name AMH				
Size A3 Partnumber: NANOC-15-11-13				
Number of sheets: 1 of 1				

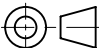






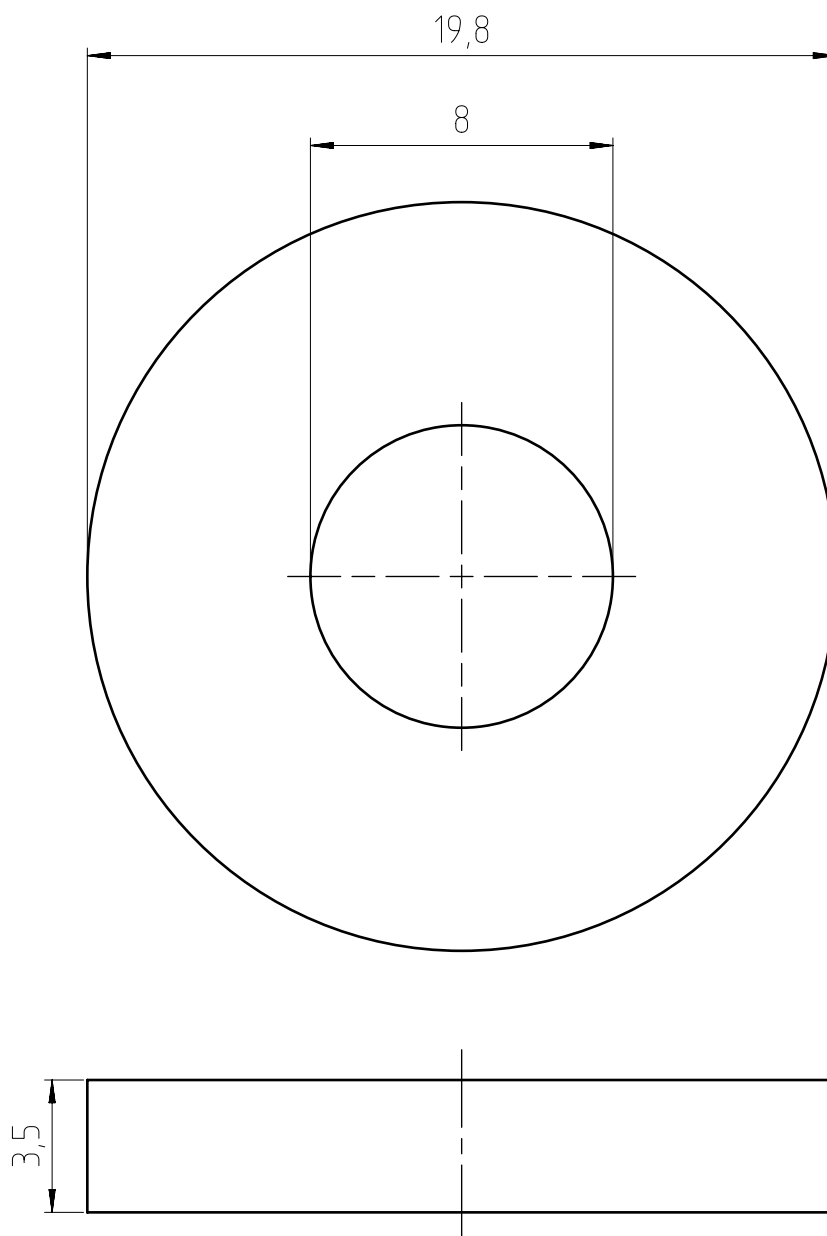
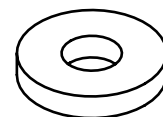
This drawing may not be used for commercial purposes without written authorisation

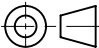

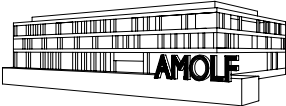
15	1	Repel spacer 1	MACOR				
Item	Qty	Partname	Material	Partnumber/Remarks			
<div>NanoCenter</div> <div>15 Verios-Simplified RFA setup</div>					Date	Name	
				DRN	15-12-2021	AMH	
				PRD	18-03-2022	AMH	
scale: 5:1		<div>010</div> <div></div>		<div></div> <div>Dim.in mm</div>	General tolerances unless otherwise specified ISO-2768-fH-E	Geometrical tolerances unless otherwise specified ISO-8015-E	Surface roughness of machined surfaces unless otherwise specified 3,2 Ra (maximum standard) 1,6 Ra (fitting typical)
<div></div> <div></div>				Size A4	Partnumber: NANOC-15-11-15		
				Number of sheets: 1 of 1			



17	1	Repel spacer 2	MACOR					
Item	Qty	Partname	Material	Partnumber/Remarks				
<div>NanoCenter</div> <div>15 Verios-Simplified RFA setup</div>					Date	Name		
				DRN	15-12-2021	AMH		
				PRD	18-03-2022	AMH		
scale: 5:1		<div>010</div> <div></div>		<div></div> <div>Dim.in mm</div>	General tolerances unless otherwise specified ISO-2768-fH-E		Geometrical tolerances unless otherwise specified ISO-8015-E	Surface roughness of machined surfaces unless otherwise specified 3,2 Ra (maximum standard 1,6 Ra (fitting typical))
<div></div> <div></div>				Size	Partnumber:			
				A4	NANOC-15-11-17			
				Number of sheets: 1 of 1				

This drawing may not be used for commercial purposes without written authorisation



19	1	Repel spacer 3	MACOR					
Item	Qty	Partname	Material	Partnumber/Remarks				
<div>NanoCenter</div> <div>15 Verios-Simplified RFA setup</div>					Date	Name		
				DRN	15-12-2021	AMH		
				PRD	18-03-2022	AMH		
scale: 5:1		<div>010</div> <div></div>		<div></div> <div>Dim.in mm</div>		General tolerances unless otherwise specified ISO-2768-FH-E	Geometrical tolerances unless otherwise specified ISO-8015-E	Surface roughness of machined surfaces unless otherwise specified 3,2 Ra (maximum standard) 1,6 Ra (fitting typical)
<div></div> <div></div>				Size A4	Partnumber: NANOC-15-11-19			
				Number of sheets: 1 of 1				

This drawing may not be used for commercial purposes without written authorisation

Bibliography

- E. Abbe. Beiträge zur theorie des mikroskops und der mikroskopischen wahrnehmung. *Archiv für mikroskopische Anatomie*, 9(1):413–468, 1873.
- B. Barwick, D. J. Flannigan, and A. H. Zewail. Photon-induced near-field electron microscopy. *Nature*, 462(7275):902–906, 2009.
- N. Brodusch, H. Demers, A. Gellé, A. Moores, and R. Gauvin. Electron energy-loss spectroscopy (eels) with a cold-field emission scanning electron microscope at low accelerating voltage in transmission mode. *Ultramicroscopy*, 203:21–36, 2019.
- F. Carbone. An electron walks into a quantum bar. . . . *Science*, 373(6561):1309–1310, 2021.
- T. Coenen and N. Haegel. Cathodoluminescence for the 21st century: Learning more from light. *Applied Physics Reviews*, 4(3):031103, 2017.
- R. Dahan, S. Nehemia, M. Shentcis, O. Reinhardt, Y. Adiv, X. Shi, O. Be’er, M. H. Lynch, Y. Kurman, K. Wang, et al. Resonant phase-matching between a light wave and a free-electron wavefunction. *Nature Physics*, 16(11):1123–1131, 2020.
- R. Dahan, A. Gorlach, U. Haeusler, A. Karnieli, O. Eyal, P. Yousefi, M. Segev, A. Arie, G. Eisenstein, P. Hommelhoff, et al. Imprinting the quantum statistics of photons on free electrons. *Science*, 373(6561):eabj7128, 2021.
- F. G. De Abajo. Optical excitations in electron microscopy. *Reviews of modern physics*, 82(1):209, 2010.
- F. J. G. de Abajo and M. Kociak. Electron energy-gain spectroscopy. *New Journal of Physics*, 10(7):073035, jul 2008. doi: 10.1088/1367-2630/10/7/073035. URL <https://doi.org/10.1088/1367-2630/10/7/073035>.
- V. Di Giulio, M. Kociak, and F. J. G. de Abajo. Probing quantum optical excitations with fast electrons. *Optica*, 6(12):1524–1534, 2019.
- R. F. Egerton et al. *Physical principles of electron microscopy*, volume 56. Springer, 2005.
- A. Feist, K. E. Echternkamp, J. Schauss, S. V. Yalunin, S. Schäfer, and C. Ropers. Quantum coherent optical phase modulation in an ultrafast transmission electron microscope. *Nature*, 521(7551):200–203, 2015.
- A. Feist, N. Bach, N. R. da Silva, T. Danz, M. Möller, K. E. Priebe, T. Domröse, J. G. Gatzmann, S. Rost, J. Schauss, et al. Ultrafast transmission electron microscopy using a laser-driven field emitter: Femtosecond resolution with a high coherence electron beam. *Ultramicroscopy*, 176:63–73, 2017.

- T. Sunaoshi, K. Kaji, Y. Orai, C. Schamp, and E. Voelkl. Stem/sem, chemical analysis, atomic resolution and surface imaging at 30 kv with no aberration correction for nanomaterials on graphene support. *Microscopy and Microanalysis*, 22(S3):604–605, 2016.
- N. Talebi. *Near-field-mediated photon-electron interactions*. Springer, 2019.
- M. van der Heijden. *Energy spread measurement of the Nano Aperture Ion Source*. Delft University of Technology, 2011.
- G. M. Vanacore, I. Madan, G. Berruto, K. Wang, E. Pomarico, R. Lamb, D. McGrouther, I. Kaminer, B. Barwick, F. J. García de Abajo, et al. Attosecond coherent control of free-electron wave functions using semi-infinite light fields. *Nature communications*, 9(1):1–11, 2018.
- K. Wang, R. Dahan, M. Shentcis, Y. Kauffmann, A. B. Hayun, O. Reinhardt, S. Tsesses, and I. Kaminer. Coherent interaction between free electrons and a photonic cavity. *Nature*, 582(7810):50–54, 2020.

List of Figures

1.1	PINEM energy spectrum of electrons measured before (left) and after (right) the interaction with the nanostructure (middle) (Feist et al., 2015).	8
1.2	Overview of the setup with the electrons indicated in blue and the laser in red.	10
1.3	Overview of the detection system, consisting of the nanostructure (chapter 2), Retarding Field Analyzer (section 3.1) and Deflection Unit (section 3.3) and the MiniPix Detector (section 3.2).	11
2.1	Simulated PINEM spectra for betas from 0 to 1 inserted into the Bessel function (Equation 2.1) with an energy spread of 0.9 eV FWHM.	14
2.2	Unit cell of the plasmonic sample with simulated field at the top surface, real parts of the E_x , E_y , E_z components and field magnitude.	15
2.3	Electron trajectories and expected PINEM energy spectra of the Plasmonic membrane for a β of 0, 0.2371 and 1.9479.	17
2.4	Simulated PINEM spectra of electron trajectories at different distances from the edge of the hole.	17
2.5	Beta squared for two membranes, only Si_3N_4 on the left and combined with gold layers on the right.	18
3.1	Simulation setup of the RFA and example of equipotential lines at an applied scanning voltage (a) below, (b) very close to and (c) above the electron energy.	20
3.2	Sharp vs gaussian distribution of initial electrons at the scanning electrode.	21
3.3	Intrinsic energy resolution (blue and orange fit) and combined with incoming electrons with a Gaussian distribution of 0.8eV (grey and violet fit) of the entire system operated at 4, 5 and 6keV.	22
3.4	Energy resolution of a sharp 6keV electron beam at starting locations from the centre.	23
3.5	Threshold sweeps of MiniPix at different electron energy settings at high sensor temperatures (around 50 degrees Celsius).	24
3.6	Cooling mechanism for the MiniPix detector with (1) Aluminium blocks, (2) copper stands and (3) the connector boat to the cryostage.	25

3.7	Left: Pole piece of the SEM and parabolic mirror which is used to couple in the laser. Right: Laser spot at different heights below the pole piece.	26
3.8	Crosscut of the structure without and with the deflection unit.	27
3.9	Simple model of electron deflection between two parallel plates (Spaldin, 2012)	28
3.10	Electron trajectories are calculated by adding electron velocities in y and z direction. The external field acts on the particle and accelerates (or decelerates) it in each step. The new spatial coordinate (s_y and s_z) are calculated with the updated velocities and used as input for the next step.	30
3.11	Lorentz factor for velocities up to the speed of light c	31
3.12	Electrostatic field magnitude and components and calculated trajectories for three electrons. Solid lines represent classical particles, dashed lines relativistic electrons. Electrons start at (0.004,+0.006) and move in negative z direction. In the initial geometry, electrons would collide with the electrodes.	32
3.13	Electrostatic field magnitude and components and calculated trajectories for three electrons. Solid lines represent classical particles, dashed lines relativistic electrons. Electrons start at (0,0) and move in negative z direction.	32
3.14	Trajectories of 5keV electrons in the deflection unit after they passed the RFA unit.	33
3.15	The new and more compact design of the deflection unit.	33
4.1	RFA imaged in the SEM with 5keV electrons while the voltage of the RFA is gradually increased.	36
4.2	RFA seen through 1000 nm pitch 500 nm hole diameters silicon nitride membrane.	37
4.3	Detected signal from the laser. Left: 0.7 mW (1 kHz, 15%) and right: 26.3 mW (25 kHz, 35%.	38
4.4	Detected signal of a scanning 5 keV electron beam at the sensor for different positions of the potentiometer, going from 0 V (a) to 2500 V (i) deflection voltage.	39
4.5	Measurements at 6 keV without and with the laser look identical.	40
4.6	Hole array of 400 nm 200 nm 2x75 nm Au, tilted 20 degrees delay sweep laser on	41
4.7	Membranes of Silicon Nitride only (left) and coated with Gold (right) damaged by laser irradiation.	42
4.8	Exposing the silicon nitride membrane to 32 mW and 38 mW laser power leads to cracking of the structure.	42
4.9	Tungsten needle after laser exposure of 1.8 mW is also heavily damaged	43

C.1	(a) A photon/electron impinges on the 200nm thick Si layer and (b) creates electron-hole pairs, which move towards the electrodes due to an applied field. (c) The signal is amplified, (d) compared to the set threshold and counted if it is above. The amount of time the signal is above the threshold is also recorded.	52
C.2	Measurements for different bias voltages	52

List of Tables

1.1	Wavelengths and velocities of electrons at different acceleration voltages . . .	7
2.1	Parameters of the two samples	15
A.1	C_2 values for different currents at spot 3.9	49
B.1	Simulation data sets of the entire RFA and deflection unit with the sample (SIMION)	51



Eidgenössische Technische Hochschule Zürich
Swiss Federal Institute of Technology Zurich

Declaration of originality

The signed declaration of originality is a component of every semester paper, Bachelor's thesis, Master's thesis and any other degree paper undertaken during the course of studies, including the respective electronic versions.

Lecturers may also require a declaration of originality for other written papers compiled for their courses.

I hereby confirm that I am the sole author of the written work here enclosed and that I have compiled it in my own words. Parts excepted are corrections of form and content by the supervisor.

Title of work (in block letters):

Authored by (in block letters):

For papers written by groups the names of all authors are required.

Name(s):

First name(s):

With my signature I confirm that

- I have committed none of the forms of plagiarism described in the '[Citation etiquette](#)' information sheet.
- I have documented all methods, data and processes truthfully.
- I have not manipulated any data.
- I have mentioned all persons who were significant facilitators of the work.

I am aware that the work may be screened electronically for plagiarism.

Place, date

Signature(s)

For papers written by groups the names of all authors are required. Their signatures collectively guarantee the entire content of the written paper.